

## Efficient conversion of syngas to linear $\alpha$ -olefins by phase-pure $\chi$ -Fe<sub>5</sub>C<sub>2</sub>

Wang, Peng; Chiang, Fu Kuo; Chai, Jiachun; Dugulan, A. Iulian; Dong, Juan; Chen, Wei; Broos, Robin J.P.; Men, Zhuowu; Hensen, Emiel J.M.; More Authors

**DOI**

[10.1038/s41586-024-08078-5](https://doi.org/10.1038/s41586-024-08078-5)

**Publication date**

2024

**Document Version**

Final published version

**Published in**

Nature

**Citation (APA)**

Wang, P., Chiang, F. K., Chai, J., Dugulan, A. I., Dong, J., Chen, W., Broos, R. J. P., Men, Z., Hensen, E. J. M., & More Authors (2024). Efficient conversion of syngas to linear  $\alpha$ -olefins by phase-pure  $\chi$ -Fe<sub>5</sub>C<sub>2</sub>. *Nature*, 635(8037), 102-107. <https://doi.org/10.1038/s41586-024-08078-5>

**Important note**

To cite this publication, please use the final published version (if applicable).  
Please check the document version above.

**Copyright**

Other than for strictly personal use, it is not permitted to download, forward or distribute the text or part of it, without the consent of the author(s) and/or copyright holder(s), unless the work is under an open content license such as Creative Commons.

**Takedown policy**

Please contact us and provide details if you believe this document breaches copyrights.  
We will remove access to the work immediately and investigate your claim.

# Efficient conversion of syngas to linear $\alpha$ -olefins by phase-pure $\chi$ -Fe<sub>5</sub>C<sub>2</sub>

<https://doi.org/10.1038/s41586-024-08078-5>

Received: 20 December 2019

Accepted: 19 September 2024

Published online: 16 October 2024

Open access

 Check for updates

Peng Wang<sup>1,2✉</sup>, Fu-Kuo Chiang<sup>1</sup>, Jiachun Chai<sup>1,2</sup>, A. Iulian Dugulan<sup>3</sup>, Juan Dong<sup>4</sup>, Wei Chen<sup>2</sup>, Robin J. P. Broos<sup>2</sup>, Bo Feng<sup>1</sup>, Yuanjun Song<sup>1,5</sup>, Yijun Lv<sup>1</sup>, Quan Lin<sup>1</sup>, Rongming Wang<sup>5</sup>, Ivo A. W. Filot<sup>2</sup>, Zhuowu Men<sup>1✉</sup> & Emiel J. M. Hensen<sup>2✉</sup>

Oil has long been the dominant feedstock for producing fuels and chemicals, but coal, natural gas and biomass are increasingly explored alternatives<sup>1–3</sup>. Their conversion first generates syngas, a mixture of CO and H<sub>2</sub>, which is then processed further using Fischer–Tropsch (FT) chemistry. However, although commercial FT technology for fuel production is established, using it to access valuable chemicals remains challenging. A case in point is linear  $\alpha$ -olefins (LAOs), which are important chemical intermediates obtained by ethylene oligomerization at present<sup>4–8</sup>. The commercial high-temperature FT process and the FT-to-olefin process under development at present both convert syngas directly to LAOs, but also generate much CO<sub>2</sub> waste that leads to a low carbon utilization efficiency<sup>9–14</sup>. The efficiency is further compromised by substantially fewer of the converted carbon atoms ending up as valuable C<sub>5</sub>–C<sub>10</sub> LAOs than are found in the C<sub>2</sub>–C<sub>4</sub> olefins that dominate the product mixtures<sup>9–14</sup>. Here we show that the use of the original phase-pure  $\chi$ -iron carbide can minimize these syngas conversion problems: tailored and optimized for the process of FT to LAOs, this catalyst exhibits an activity at 290 °C that is 1–2 orders higher than dedicated FT-to-olefin catalysts can achieve above 320 °C (refs. 12–15), is stable for 200 h, and produces desired C<sub>2</sub>–C<sub>10</sub> LAOs and unwanted CO<sub>2</sub> with carbon-based selectivities of 51% and 9% under industrially relevant conditions. This higher catalytic performance, persisting over a wide temperature range (250–320 °C), demonstrates the potential of the system for developing a practically relevant technology.

With iron carbide as the active phase in iron-based FT catalysts, earlier work has explored the stability of different carbide phases<sup>16–18</sup> and shown that phase-pure  $\epsilon$ -iron carbide does not produce CO<sub>2</sub> as a primary product unlike typical iron-based FT catalysts<sup>16</sup>. Informed by this and aiming for an active phase that can be operated in a stable manner in a broad temperature range required for optimization of the FT-to-LAO (FTLAO) process, we focused on obtaining phase-pure  $\chi$ -iron carbide<sup>16–18</sup>. Different from the procedure to obtain pure  $\epsilon$ -iron carbide, passivation of fully reduced Raney iron before carburization in syngas yielded phase-pure  $\chi$ -iron carbide without competing iron oxide phases.

Table 1 compares the FTLAO performance of our  $\chi$ -iron carbide ( $\chi$ -Fe<sub>5</sub>C<sub>2</sub>) against that of other catalysts, which illustrates the high activity of our system. Already at 250 °C, the CO conversion time yield (CTY) is 3–7 times higher than that of all the state-of-the-art catalysts from the literature<sup>13–15,19,20</sup>, which were typically evaluated at substantially higher reaction temperatures above 320 °C. At 250 °C, we also observe a low CO<sub>2</sub> selectivity of 11% and associated high overall carbon efficiency (selectivity to hydrocarbons and oxygenates) of 89%. Table 1 shows that with few exceptions, the reference catalysts exhibit a much higher

CO<sub>2</sub> selectivity ranging from 37% to 47% and a lower carbon efficiency ranging from 63% to 53% (refs. 13,14,19). Despite the low CO<sub>2</sub> selectivity of 13% obtained with a hydrophobic FeMn@Si catalyst, this system shows a lower activity, even at a much higher reaction temperature of 320 °C. Although more expensive catalysts based on cobalt carbide are active in the same low-temperature range as our catalyst, typical CTY values are still substantially lower at an unfavourable CO<sub>2</sub> selectivity close to 50% (ref. 19). In terms of CO<sub>2</sub> selectivity, Co<sub>1</sub>Mn<sub>3</sub>–Na<sub>2</sub>S exhibits a notably low value of less than 3% at 240 °C that, however, increases rapidly as the temperature is ramped up to improve the activity<sup>20</sup>. We also note that, as discussed in the literature<sup>21,22</sup>, operation at elevated temperatures shifts the product distribution of cobalt-based catalysts towards less desired products and renders them more susceptible to poisoning.

We used density functional theory calculations and microkinetic simulations to explore FT chemistry as catalysed by  $\chi$ -Fe<sub>5</sub>C<sub>2</sub> (see Methods, Extended Data Figs. 1 and 2 and Extended Data Table 1 for full details), finding the expected exponential increase in CO conversion and hydrocarbon formation rates with temperature and a C<sub>2+</sub> hydrocarbon distribution according to Anderson–Schulz–Flory (ASF) theory

<sup>1</sup>CTL Technology Research Center, National Institute of Clean-and-Low-Carbon Energy, CHN Energy, Beijing, People's Republic of China. <sup>2</sup>Laboratory of Inorganic Materials and Catalysis, Department of Chemical Engineering and Chemistry, Eindhoven University of Technology, Eindhoven, The Netherlands. <sup>3</sup>Fundamental Aspects of Materials and Energy Group, Delft University of Technology, Delft, The Netherlands. <sup>4</sup>Data Technology Group, China Energy Investment Group Archives, CHN Energy, Beijing, People's Republic of China. <sup>5</sup>Beijing Advanced Innovation Center for Materials Genome Engineering, Beijing Key Laboratory for Magneto-Photoelectrical Composite and Interface Science, State Key Laboratory for Advanced Metals and Materials, University of Science and Technology Beijing, Beijing, People's Republic of China. ✉e-mail: peng.wang.hm@chnenergy.com.cn; zhuowu.men@chnenergy.com.cn; e.j.m.hensen@tue.nl

**Table 1 | Catalytic performance comparison of FTLAO and reported catalysts**

Sample	T (°C)	CO conversion (%)	Carbon efficiency <sup>a</sup> (%)	P (MPa) <sup>b</sup>	SV (ml g <sup>-1</sup> cat <sup>-1</sup> h <sup>-1</sup> ) <sup>c</sup>				O/P ratio <sup>d</sup>	Carbon-based selectivity (%)		Catalyst time yield (μmol g <sup>-1</sup> cat <sup>-1</sup> s <sup>-1</sup> )		
					H <sub>2</sub>	CO	Inert gas	Total		H <sub>2</sub> /CO ratio	CO <sub>2</sub>	Target olefins <sup>e</sup>	CO	Target olefins <sup>e</sup>
χ-Fe <sub>5</sub> C <sub>2</sub> (this work)	250	27.8	88.8	2.3	12,000	8,000	8,000	28,000	1.5	1.2	11.2	24.3	27.6	6.7
Mn-χ-Fe <sub>5</sub> C <sub>2</sub> (this work)	250	16.0	90.7	2.3	12,000	8,000	8,000	28,000	1.5	4.1	9.3	50.7	15.9	8.0
Mn-χ-Fe <sub>5</sub> C <sub>2</sub> (this work)	250	46.1	90.6	3.0	3,000	1,900	100	5,000	1.5	4.1	9.4	48.5	10.9	5.3
Mn-χ-Fe <sub>5</sub> C <sub>2</sub> (this work)	290	70.7	78.1	2.5	18,000	11,400	600	30,000	1.5	4.5	21.9	42.0	100.0	42.0
Mn-χ-Fe <sub>5</sub> C <sub>2</sub> (this work)	290	52.8	79.2	2.5	36,000	22,800	1,200	60,000	1.5	4.6	20.8	43.6	149.3	65.1
Mn-χ-Fe <sub>5</sub> C <sub>2</sub> (this work)	320	91.2	68.0	2.5	36,000	22,800	1,200	60,000	1.5	2.7	32.0	28.5	257.9	73.5
Na <sub>2</sub> S-Fe-CNF (ref. 13)	340	88.0	58.0	2.0	328.5	328.5	73	730	1.0	4.3	42.0	30.2	3.6	1.1
FeMn@Si (ref. 15)	320	56.1	87.0	2.0	2,533	1,267	200	4,000	2.0	5.1	13.0	44.0	8.8	3.9
Mn-Na-Co <sub>2</sub> C (ref. 19)	250	28.6	53.4	1.0	647	1,293	60	2,000	0.5	5.6	46.6	17.0	4.6	0.8
Co <sub>3</sub> Mn <sub>3</sub> -Na <sub>2</sub> S (ref. 20)	240	18	>97	1.0	4,800	2,400	800	8,000	2.0	4.3	<3	29.0	5.4	1.6
	280	20	79.0	1.0	4,800	2,400	800	8,000	2.0	2.0	21.0	17.4	6.0	1.0
Fe-Al <sub>2</sub> O <sub>3</sub> (SCS350) <sup>f</sup> (ref. 14)	320	22.1	63.3	1.5	3,000	3,000	-	6,000	1.0	0.4	36.7	9.1	8.2	0.7
Fe-Al <sub>2</sub> O <sub>3</sub> (SAP) <sup>f</sup> (ref. 14)	436	21.4	63.3	1.5	3,000	3,000	-	6,000	1.0	1.3	36.7	11.6	8.0	0.9
Fe-Al <sub>2</sub> O <sub>3</sub> (SCP) <sup>f</sup> (ref. 14)	500	18.3	58.9	1.5	3,000	3,000	-	6,000	1.0	2.7	41.1	25.4	6.8	1.7

The data shown are for a fixed-bed reactor; CTY represents the number of moles of converted CO or moles of produced target olefins per gram of catalyst per second; carbon efficiency is the fraction of C atoms from CO converted ending up in hydrocarbons and oxygenates.

<sup>a</sup>Overall carbon-based selectivity of hydrocarbon and oxygenate products.

<sup>b</sup>Reaction pressure.

<sup>c</sup>Syngas (H<sub>2</sub>+CO) SV.

<sup>d</sup>For Mn-χ-Fe<sub>5</sub>C<sub>2</sub>, χ-Fe<sub>5</sub>C<sub>2</sub> and FeMn@Si, the value refers to the O/P ratio in C<sub>2</sub>-C<sub>10</sub> products. For other samples, it refers to the O/P ratio in C<sub>2</sub>-C<sub>4</sub> products.

<sup>e</sup>For Mn-χ-Fe<sub>5</sub>C<sub>2</sub>, χ-Fe<sub>5</sub>C<sub>2</sub> and FeMn@Si, target olefins are C<sub>2</sub>-C<sub>10</sub> LAOs. For other samples, target olefins are light olefins (C<sub>2</sub>-C<sub>4</sub>).

<sup>f</sup>SCS350, SAP and SCP are the catalyst sample codes used in ref. 14.

(Extended Data Figs. 1a and 2a). Simulated olefin-to-paraffin (O/P) ratios are in the same range as the experimentally observed ratios and exhibit a minor dependence on temperature (Extended Data Fig. 2c), indicating that both olefins and paraffins are primary products. The calculations also show that for χ-Fe<sub>5</sub>C<sub>2</sub>, the energy barrier for H<sub>2</sub>O formation is lower than that for CO<sub>2</sub> formation and that oxygen from CO dissociation will thus be removed primarily as water, which explains the low CO<sub>2</sub> selectivity of our system. This observation also explains the importance of using a phase-pure catalyst: incomplete conversion of the catalyst precursor to χ-Fe<sub>5</sub>C<sub>2</sub> will result in the presence of competing phases that often include iron oxides, which are known as good catalysts for the water-gas shift reaction that generates CO<sub>2</sub> from CO and water<sup>23</sup>.

High-resolution transmission electron microscopy (HRTEM) imaging indicates that very little amorphous carbon is deposited on the phase-pure χ-iron carbide, which contributes to its high and stable CO conversion rate and low CO<sub>2</sub> selectivity (Extended Data Fig. 3a). This contrasts with the substantial level of carbon deposition onto the surface of a catalyst containing 86% χ-Fe<sub>5</sub>C<sub>2</sub> and iron oxide phases (Extended Data Fig. 3b), which was reported<sup>24</sup> to reach a high CO CTY of 303 μmol g<sup>-1</sup> s<sup>-1</sup> but also a high CO<sub>2</sub> selectivity of 45% at a temperature of 340 °C. As this catalyst used potassium<sup>24</sup> as a promoter known to improve CO conversion, we also promoted our phase-pure χ-Fe<sub>5</sub>C<sub>2</sub> with potassium and achieved at a lower temperature of 325 °C a higher CO CTY of 570 μmol (g<sup>-1</sup> s<sup>-1</sup>), lower CO<sub>2</sub> selectivity of 37% and better stability (Extended Data Fig. 3c). Our phase-pure χ-Fe<sub>5</sub>C<sub>2</sub> catalyst thus outperforms the phase-impure χ-Fe<sub>5</sub>C<sub>2</sub> catalyst in terms of activity and CO<sub>2</sub> selectivity, although the better performance will also in part be due to differences in catalyst particle size (about 17 nm for our catalyst, see Extended Data Fig. 7i, versus about 3 nm reported<sup>24</sup> for the phase-impure catalyst)<sup>25</sup>. To achieve a high carbon efficiency and high LAO yields, we opted to not use potassium promoters that inevitably increase the CO<sub>2</sub> selectivity.

However, despite the competitive performance, the O/P ratio and the fraction of LAOs among total olefins obtained with the phase-pure

χ-Fe<sub>5</sub>C<sub>2</sub> catalyst are still relatively low and limit the carbon-based selectivity towards desirable C<sub>2</sub>-C<sub>10</sub> LAOs to 25%. Mechanistically, this is attributed to olefins, which are the primary products of the FT reaction, re-adsorbing and undergoing hydrogenation and isomerization reactions that convert them into less valuable paraffins and iso-olefins. As the addition of manganese is known to improve the activity and product selectivity of iron-based FT catalysts<sup>26</sup>, we promoted the phase-pure χ-Fe<sub>5</sub>C<sub>2</sub> catalyst with manganese (Mn-χ-Fe<sub>5</sub>C<sub>2</sub>) and achieved the highest O/P ratio and lowest CO<sub>2</sub> selectivity at an optimized manganese content of 10% by weight (Extended Data Figs. 4a-e and 5a). Although blocking of active sites by manganese slightly lowers the CO CTY for Mn-χ-Fe<sub>5</sub>C<sub>2</sub>, the promoted catalyst still outperforms all reported catalysts and maintains its high phase purity and associated low CO<sub>2</sub> selectivity while exhibiting a much improved product distribution (entries 1-3 of Table 1): the O/P ratio of C<sub>2</sub>-C<sub>10</sub> olefins and the selectivity to target LAOs increase from 1.2 to 4.1 and 24.3% to 50.7%, respectively. In analogy with the manganese promotion effect seen in cobalt-based FT catalysts<sup>26</sup>, these changes are probably due to the stronger CO adsorption compared with H<sub>2</sub>.

The FT product distribution is typically strongly affected by the CO conversion, with higher conversions increasing the CO<sub>2</sub> selectivity and decreasing the olefin selectivity and O/P ratio<sup>27,28</sup>. This trend is attributed to the water-gas shift reaction involving initially formed water and hydrogenation of initially formed olefins, with both processes becoming more pronounced as the residence time of reactants and therefore also of initial products in the reactor increases to enable higher CO conversions. Extended Data Table 2 illustrates this by showing how the CO<sub>2</sub> selectivity of the Mn-χ-Fe<sub>5</sub>C<sub>2</sub> catalyst (manganese-promoted phase-pure χ-Fe<sub>5</sub>C<sub>2</sub>) varies with CO conversion, which depends on temperature and the flow rate of reactants through the reactor.

We next explored the performance of Mn-χ-Fe<sub>5</sub>C<sub>2</sub> under a range of reaction conditions relevant to industrial practice by varying the temperature between 250 °C and 320 °C and the space velocity (SV; the rate at which reactants are fed into the reactor) between 5,000 and

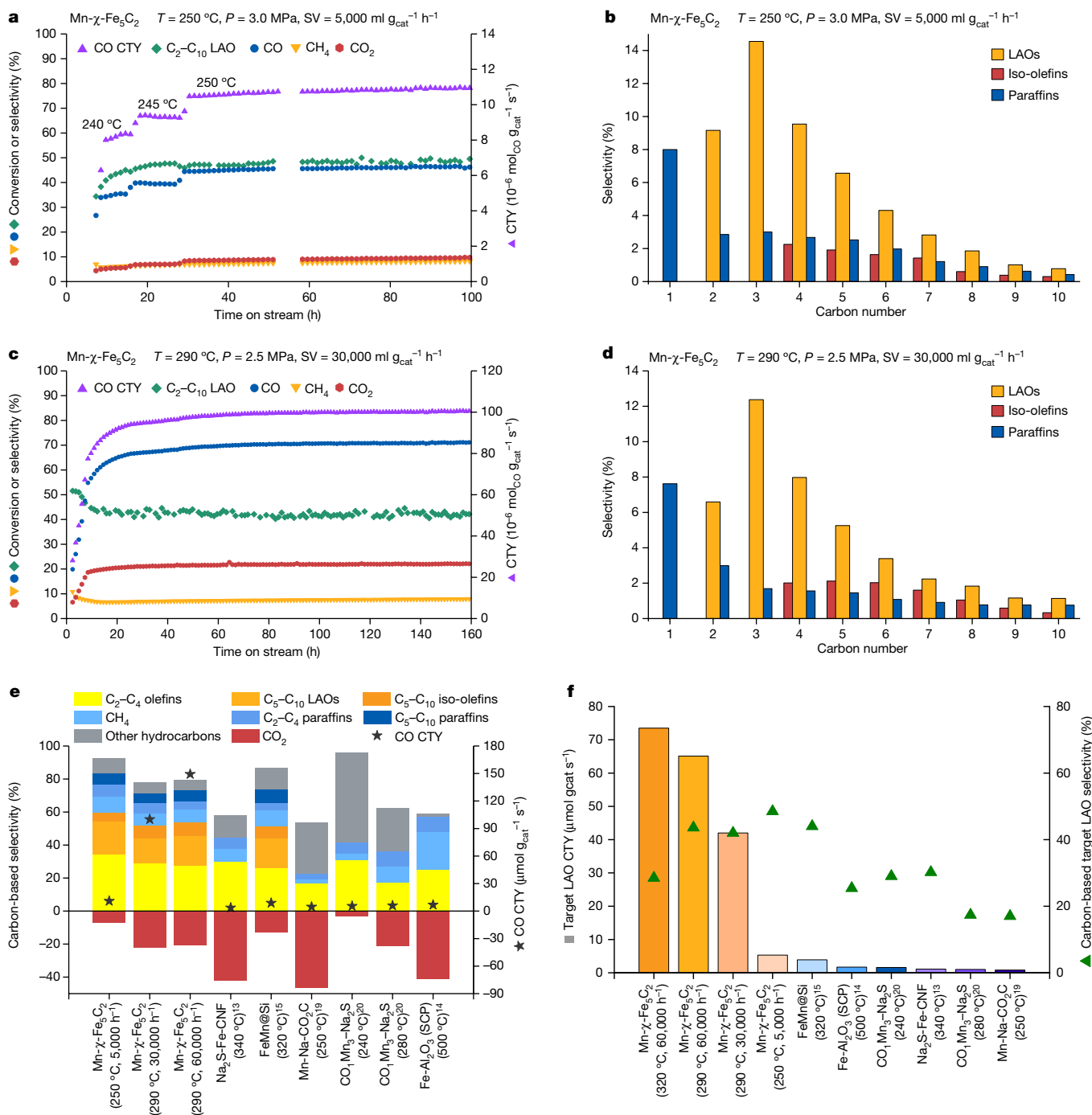


**Fig. 1 | Catalytic performance of optimized Mn- $\chi$ -Fe<sub>5</sub>C<sub>2</sub>.** **a, b**, CO conversion and product selectivity with time on stream (**a**) and averaged product distribution (**b**) at 3.0 MPa, 250 °C and SVH<sub>2</sub>/CO/Ar = 3,000/1,900/100 ml g<sub>cat</sub><sup>-1</sup> h<sup>-1</sup>. **c, d**, CO conversion and product selectivity with time on stream (**c**) and

averaged product distribution (**d**) at 2.5 MPa, 290 °C and SV H<sub>2</sub>/CO/Ar = 18,000/11,400/600 ml g<sub>cat</sub><sup>-1</sup> h<sup>-1</sup>. **e, f**, Comparison of the distribution of carbon-based products (**e**) and target LAO time yield and carbon-based LAO selectivity (**f**) between Mn- $\chi$ -Fe<sub>5</sub>C<sub>2</sub>,  $\chi$ -Fe<sub>5</sub>C<sub>2</sub> and reported catalysts from Table 1.

60,000 ml g<sub>cat</sub><sup>-1</sup> h<sup>-1</sup>) while keeping the pressures at 2.5–3.0 MPa and the H<sub>2</sub>/CO ratio at 1.5 (Table 1, rows 3–6). Table 1 provides an overview of performance data of the top-performing catalyst systems for converting syngas to olefins (and thus excludes potassium-promoted systems). Various reactions conditions (with respect to temperature, pressure, H<sub>2</sub>/CO ratio and contact time) were selected for the systems listed, to ensure the best results in terms of olefin yield. The comparison shows that our Mn- $\chi$ -Fe<sub>5</sub>C<sub>2</sub> catalyst outperforms other catalysts reported in the literature in terms of CO conversion and a low CO<sub>2</sub> selectivity that implies a high selectivity to desired LAOs. We note, however, that the

comparison does not take into account the effect of catalyst particle size differences known to affect<sup>25</sup> performance, owing to lack of data.

Using a relatively low temperature of 250 °C, a pressure of 3.0 MPa and an SV of 5,000 ml g<sub>cat</sub><sup>-1</sup> h<sup>-1</sup> (Fig. 1a and Table 1), we achieved a constant CO conversion of about 46% over 100 h with an exceptionally low CO<sub>2</sub> selectivity of 9.4%, a high carbon-based selectivity towards C<sub>2</sub>–C<sub>10</sub> LAOs of 48.5% and a CO CTY of 10.9  $\mu\text{mol g}_{\text{cat}}^{-1}\text{ s}^{-1}$ . Using a slightly higher but still moderate temperature of 290 °C, a pressure of 2.5 MPa and an SV of 30,000 ml g<sub>cat</sub><sup>-1</sup> h<sup>-1</sup> (Fig. 1c and Table 1) that resulted in less favourable CO<sub>2</sub> selectivity (21.9%) and target LAO selectivity (42.0%), we

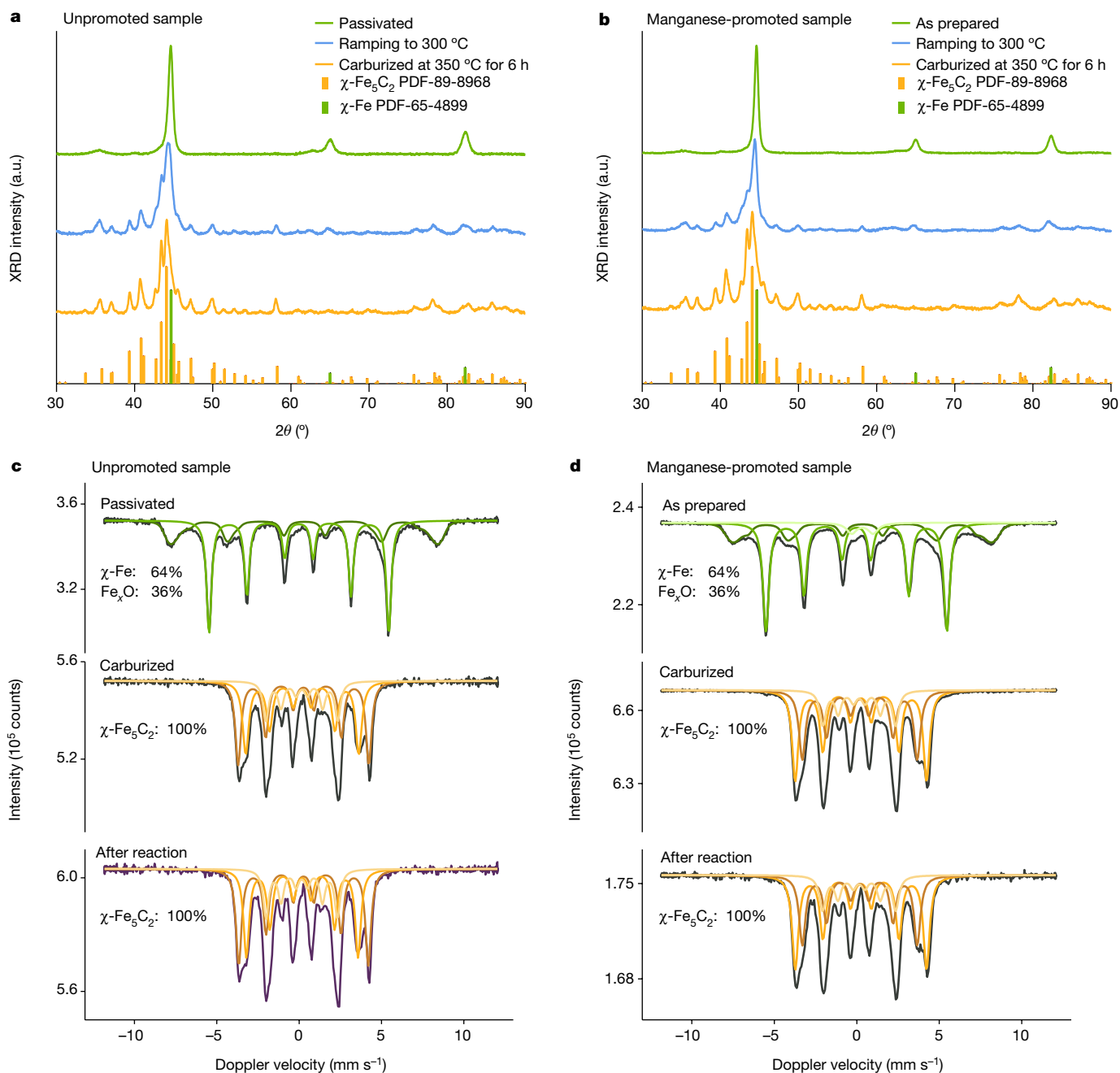


**Fig. 2 | In situ characterization of active-phase formation and evolution.** **a,b**, In situ XRD patterns of the transformation of unpromoted (**a**) and Mn-promoted (**b**) Raney iron, showing carburization at 300 °C and 350 °C for 6 h (carburization:  $H_2/CO = 30$ , 0.1 MPa, heating from 30 °C to 350 °C at 0.5 °C  $min^{-1}$ , dwell 6 h). a.u., arbitrary units. **c,d**, In situ Mössbauer spectra of the

transformation of unpromoted (**c**) and Mn-promoted (**d**) Raney iron, showing as-prepared, after carburization and after FT/LAO reaction (carburization:  $H_2/CO/He = 100/3.2/21.8$ , 0.1 MPa, 350 °C for 6 h; FT/LAO reaction:  $H_2/CO = 1.5$  with saturated vapour water (about 0.8 bar) at a total pressure of 2.3 MPa, 265 °C for 12 h). The Mössbauer spectra were acquired at -153 °C.

achieved an almost tenfold higher CO CTY of  $100.0 \mu mol g_{cat}^{-1} s^{-1}$  at a stable and high CO conversion of 70.7%. The average carbon-based selectivities of LAOs, iso-olefins and paraffins under these two operating conditions are shown in Fig. 1b,d. The amount of higher hydrocarbons follows the ASF distribution. The decrease in the ratio of LAOs to iso-olefins with increasing carbon number (Extended Data Fig. 5b) is attributed to consecutive reactions that preferentially convert the heavier products that reside for a longer time in the reactor<sup>29,30</sup>.

An advantage of operating at a moderate temperature is the high CO conversion achieved at a high SV of  $60,000 ml g_{cat}^{-1} h^{-1}$  at 2.5 MPa with a high CTY towards LAOs. The highest CO CTY is achieved at our highest temperature of 320 °C with a pressure of 2.5 MPa and an SV of

$60,000 ml g_{cat}^{-1} h^{-1}$ , with  $CO_2$  selectivity also increasing to 32% but still remaining substantially below values reported in the literature for FT catalysts operated under harsh conditions in Table 1. The increase in  $CO_2$  selectivity is a natural consequence of high CO conversion levels while using a  $H_2/CO$  feed ratio of 1.5, which will deplete  $H_2$  and thereby suppress removal of oxygen from CO dissociation in the form of  $H_2O$  and allow  $CO_2$  formation instead. Although  $H_2/CO$  ratios ranging from 0.5 to 2.0 are common for FT performance evaluations (Table 1), we kept the ratio constant at 1.5 for all of our experiments because a  $H_2/CO$  ratio of between 1 and 2 represents the composition of commercial syngas feeds. A higher  $H_2/CO$  ratio affects the FT performance mainly through higher CO conversion and lower  $CO_2$  selectivity (due to the

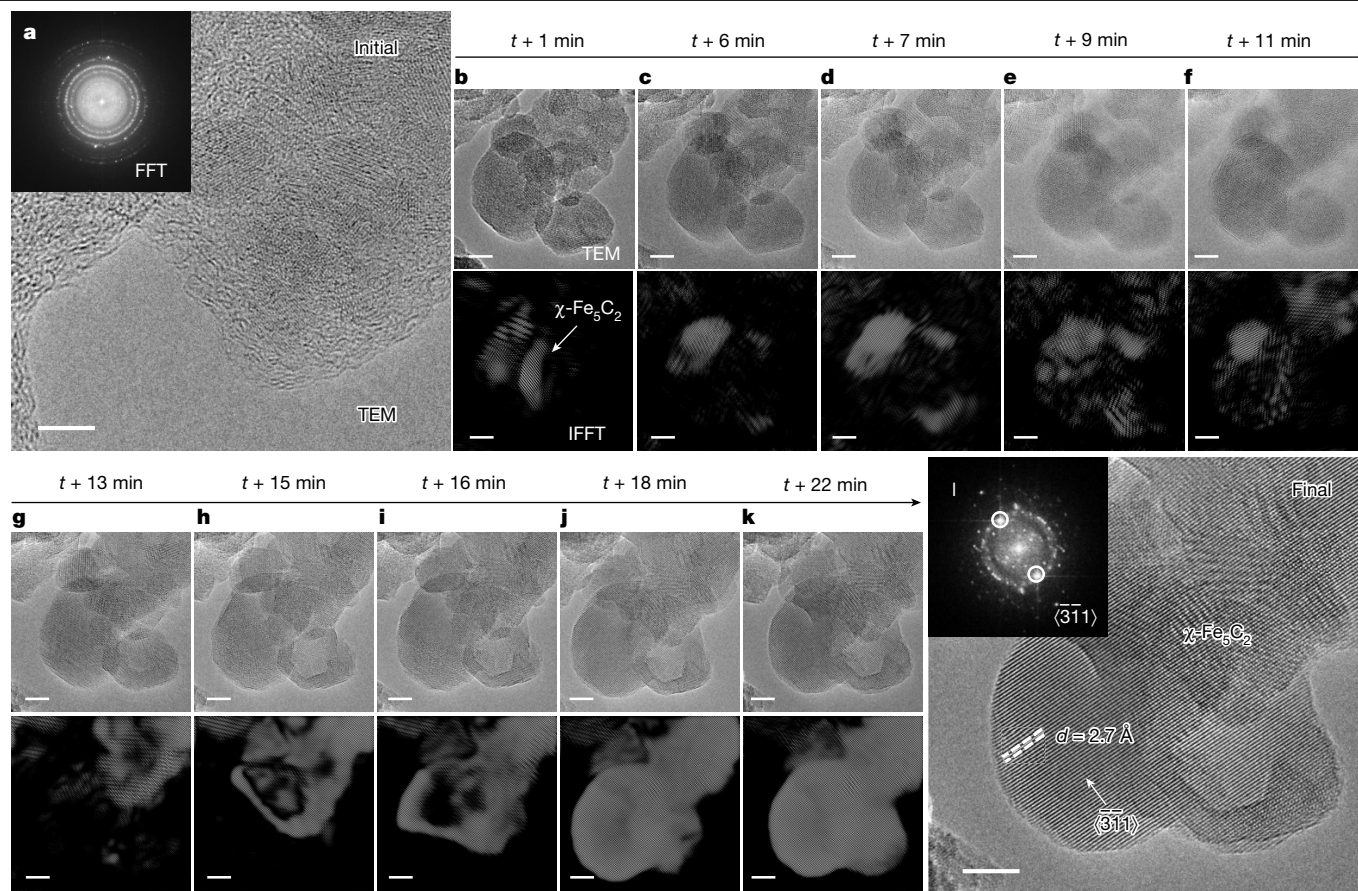


**Fig. 3 | Environmental TEM study of phase-pure  $\chi$ -Fe<sub>5</sub>C<sub>2</sub> formation.** a–l, HRTEM images of the transformation from the initial state of Raney iron (a), through carburization (b–k) to the final state (l). The dashed lines in l mark the lattice spacing of  $\chi$ -Fe<sub>5</sub>C<sub>2</sub>. The corresponding inverse fast Fourier transform

(IFFT) images show the location of  $\chi$ -Fe<sub>5</sub>C<sub>2</sub> in real space (environmental TEM conditions: H<sub>2</sub>/CO = 30, 1,200 Pa, 350 °C). FFT, fast Fourier transform. Scale bars, 5 nm.

competition of oxygen removal as CO<sub>2</sub> and H<sub>2</sub>O just mentioned<sup>31</sup>). Our phase-pure Mn- $\chi$ -Fe<sub>5</sub>C<sub>2</sub> catalyst exhibits a higher CO conversion and a lower CO<sub>2</sub> selectivity than those of the top-performing catalysts at a H<sub>2</sub>/CO ratio of 2.0, emphasizing the high performance of our catalyst, which is maintained over a range of operating conditions.

The ASF distribution predicts that a probability  $\alpha$  of about 0.63 for further growth of a hydrocarbon chain versus termination will yield the highest fraction of C<sub>2</sub>–C<sub>10</sub> hydrocarbons of 81% (Extended Data Fig. 6a). Careful product analysis (Extended Data Fig. 6b) shows that the experimentally determined values of  $\alpha$  for our catalyst are close to this optimum: 0.61 and 0.63 at reaction temperatures of 250 and 290 °C, respectively, with corresponding experimentally obtained fractions of C<sub>2</sub>–C<sub>10</sub> products of 83.1% and 81.5% that are close to the predicted ASF value. The performance of our optimized Mn- $\chi$ -Fe<sub>5</sub>C<sub>2</sub> catalyst is also notable for producing much less CH<sub>4</sub> than predicted by the ASF distribution and generating substantial amounts of more valuable reaction products. Figure 1e plots the CTY and carbon-based selectivity for Mn- $\chi$ -Fe<sub>5</sub>C<sub>2</sub> and reported catalysts in Table 1, with valuable reaction products as positive contributions and undesirable CO<sub>2</sub> as the negative one. Mn- $\chi$ -Fe<sub>5</sub>C<sub>2</sub> operated at 250 °C exhibits the highest selectivity to lower olefins (slightly higher than the selectivity reported for Na<sub>2</sub>S-promoted Fe-CNF at 340 °C)<sup>13</sup> while also generating 20% of products in the form of valuable LAOs. At 290 °C, Mn- $\chi$ -Fe<sub>5</sub>C<sub>2</sub> shows a similar selectivity to C<sub>2</sub>–C<sub>10</sub> LAOs and a 10–15 times higher CTY compared to that of FeMn@Si (ref. 15). The exceptionally low CO<sub>2</sub> selectivity for our catalyst (9%) is highly advantageous for processes targeting chemicals such as LAOs as the manganese promoter suppresses hydrogenation and thereby increases the O/P ratio of the C<sub>2</sub>–C<sub>10</sub> products to high

values between 4.1 and 4.6. This, in conjunction with the near-optimum  $\alpha$  value, ensures that Mn- $\chi$ -Fe<sub>5</sub>C<sub>2</sub> realizes a carbon-based selectivity towards desirable LAOs that is close to 50%. Moreover, the optimized Mn- $\chi$ -Fe<sub>5</sub>C<sub>2</sub> catalyst operated at a pressure of 2.5 MPa, an SV of 60,000 ml g<sub>cat</sub><sup>-1</sup> h<sup>-1</sup> and temperatures of 290 or 320 °C achieves a 10- to nearly 100-fold higher LAO CTY than those of the top-performing catalysts described in the literature and operated at similar or higher reaction temperatures (Fig. 1f).

Given the critical importance of phase purity for the performance of the  $\chi$ -Fe<sub>5</sub>C<sub>2</sub> catalyst, we monitored in situ the formation of the phase-pure material from the catalyst precursor pre-treated and activated in the reactor. We used a method differing from that for the preparation of phase-pure  $\epsilon$ -Fe<sub>5</sub>C<sub>x</sub> (ref. 16), in which we passivated Raney iron, after reduction and before carburization, in 1% O<sub>2</sub> in He at room temperature for 20 h and then carried out carburization into  $\chi$ -Fe<sub>5</sub>C<sub>2</sub> by simple exposure to a H<sub>2</sub>/CO/He mixture (100/3.2/21.8) and heating in the reactor (0.5 °C min<sup>-1</sup>, 350 °C, 6 h dwell). The in situ X-ray diffraction (XRD) patterns in Fig. 2a show that  $\chi$ -Fe<sub>5</sub>C<sub>2</sub> (Hägg carbide) formation started at 300 °C and was completed after 6 h at 350 °C. Active-phase formation proceeds in the same way in the presence of a manganese promoter (Fig. 2b). This method to prepare phase-pure  $\chi$ -Fe<sub>5</sub>C<sub>2</sub> has considerable advantages over methods in the literature<sup>12,13,17,24,32</sup>; it can be carried out in situ by using just a syngas feed with an adjusted H<sub>2</sub>/CO ratio in a single pretreatment step.

We followed the formation of  $\chi$ -Fe<sub>5</sub>C<sub>2</sub> during the carburization process in an environmental transmission electron microscope<sup>33</sup>. HRTEM images and corresponding filtered inverse fast Fourier transform images in Fig. 3 show that the passivated Raney iron is initially present

as crystallized iron particles surrounded by an amorphous oxide passivation layer (Fig. 3a). Exposure to syngas at a  $H_2/CO$  ratio of 30 at 1,200 Pa and 350 °C in the environmental transmission electron microscope initiates the  $\chi\text{-Fe}_5\text{C}_2$  formation captured by the images shown in Fig. 3b–l. The transformation is seen to start at the inner layers of Raney iron and then extends over the whole region until the final state is reached 30 min later ( $t + 30$  min) and a phase-pure  $\chi\text{-Fe}_5\text{C}_2$  grain is imaged along the  $(\bar{3}\bar{1}\bar{1})$  direction with a characteristic lattice spacing of about 2.7 Å (Fig. 3l). Carburization takes place quickly and completes the transformation into  $\chi\text{-Fe}_5\text{C}_2$  in less than 0.5 h at a low CO partial pressure of 40 Pa (Supplementary Video 1). This is in line with the in situ XRD data and underpins the efficiency of our approach to preparing  $\chi\text{-Fe}_5\text{C}_2$ , compared to alternatives that use pure CO or syngas with a much lower  $H_2/CO$  ratio of 2 (Extended Data Fig. 7).

We duplicated the carburization procedure inside a high-pressure Mössbauer spectroscopy set-up to monitor in situ the stability of phase-pure  $\chi\text{-Fe}_5\text{C}_2$  catalysts under reaction conditions. Figure 2c,d confirms the purity of the  $\chi\text{-Fe}_5\text{C}_2$  phase in unpromoted and manganese-promoted catalysts after carburization and subsequent operation under FT reaction conditions. In all samples, Hägg carbide ( $\chi\text{-Fe}_5\text{C}_2$ ) is the only iron phase present (Extended Data Table 3); that is, it is stable during prolonged operation under FT-LAO conditions (Fig. 1a,c) at 265 °C. Characterization of a used Mn- $\chi\text{-Fe}_5\text{C}_2$  sample by transmission electron microscopy (TEM) shows a well-maintained  $\chi\text{-Fe}_5\text{C}_2$  phase, without signs of carbon deposition or migration of manganese from the iron phase (Extended Data Fig. 4f–j). This is in line with a recent study<sup>34</sup> showing that manganese suppresses carbon deposition and improves the removal of oxygen, effectively cleaning the surface, which can also explain the high stability we observe. Direct long-term catalytic testing at 320–325 °C, 2.3 MPa and an SV of 100,000 ml<sub>syngas</sub> g<sub>cat</sub><sup>-1</sup> h<sup>-1</sup> shows stable Mn- $\chi\text{-Fe}_5\text{C}_2$  performance over 225 h, with a high CO conversion of 53% and a CTY of 265  $\mu\text{mol g}_{\text{cat}}^{-1} \text{s}^{-1}$  (Extended Data Fig. 5c). From the catalytic data, it follows that the water pressure under these reaction conditions will be at most 0.12 MPa, which is well below the minimum water pressure at which the disadvantageous oxidation of Hägg carbide takes places<sup>35</sup>.

Taken together, our in situ characterization and catalytic data show that phase-pure  $\chi\text{-Fe}_5\text{C}_2$  catalysts (both unpromoted and manganese-promoted) are stable and very active for FT-LAO. The phase purity of  $\chi\text{-Fe}_5\text{C}_2$  enables high CO conversion already at mild conditions and minimizes unwanted CO<sub>2</sub> production, and manganese promotion inhibits unwanted secondary reactions and thereby contributes to the high selectivity towards desired LAOs. Although industrialization of catalysts inevitably requires addressing process engineering challenges (such as, in this case, catalyst exposure to recycled feed that would include CO<sub>2</sub> and thereby increase water production), we believe phase-pure  $\chi\text{-Fe}_5\text{C}_2$  catalysts will be beneficial in the development of an FT-LAO process for converting syngas to valuable LAOs in a competitive manner<sup>9</sup>. Given the demonstrated ability of this type of catalyst to convert CO with high carbon efficiency (that is, low CO<sub>2</sub> selectivity), we anticipate that it could also benefit other applications that target, for instance, the production of alcohols, aromatics or jet fuels from syngas derived from conventional or renewable carbon feedstock.

## Online content

Any methods, additional references, Nature Portfolio reporting summaries, source data, extended data, supplementary information, acknowledgements, peer review information; details of author contributions and competing interests; and statements of data and code availability are available at <https://doi.org/10.1038/s41586-024-08078-5>.

- Dudley, B. & Dale, S. *BP Statistical Review of World Energy* (2012).
- Biról, F. & Besson, C. *Golden Rules for a Golden Age of Gas, World Energy Outlook Special Report on Unconventional Gas* (International Energy Agency, 2012).

- McFarland, E. Unconventional chemistry for unconventional natural gas. *Science* **338**, 340–342 (2012).
- Weissermel, K. & Arpe, H. *Industrial Organic Chemistry, Important Raw Materials and Intermediates* (Verlag Chemie, 1978).
- Tobisch, S. & Ziegler, T. Catalytic oligomerization of ethylene to higher linear  $\alpha$ -olefins promoted by the cationic group 4 [( $\eta$ -6-Cp-(CMe<sub>2</sub>-bridge)-Ph)M<sup>+</sup>(ethylene)<sub>2</sub>]<sup>+</sup>(M = Ti, Zr, Hf) active catalysts: a density functional investigation of the influence of the metal on the catalytic activity and selectivity. *J. Am. Chem. Soc.* **126**, 9059–9071 (2004).
- Belov, G. Tetramerization of ethylene to octene-1 (a review). *Pet. Chem.* **52**, 139–154 (2012).
- Rogers, J. S. & Bazan, G. C. Oligomerization–transmetalation reactions of Cp\* CrMe<sub>2</sub> (PMe<sub>3</sub>)/methylaluminoxane catalysts. *Chem. Commun.* **2**, 1209–1210 (2000).
- Hulea, V. & Fajula, F. Ni-exchanged Al MCM-41-An efficient bifunctional catalyst for ethylene oligomerization. *J. Catal.* **225**, 213–222 (2004).
- de Klerk, A. *Fischer-Tropsch Refining* (Wiley, 2012).
- de Klerk, A. Fischer-Tropsch refining: technology selection to match molecules. *Green Chem.* **10**, 1249–1279 (2008).
- Maitlis, P. M. & de Klerk, A. *Greener Fischer-Tropsch Processes: For Fuels and Feedstocks* (Wiley, 2013).
- Baker, B. G., Clark, N. J., McArthur, H. & Summerville, E. Catalysts and methods of their manufacture. US patent 4,610,975 (1986).
- Torres Galvis, H. M. et al. Supported iron nanoparticles as catalysts for sustainable production of lower olefins. *Science* **335**, 835–838 (2012).
- Barrault, J., Forquy, C., Menezo, J. & Maurel, R. Selective hydrocondensation of CO to light olefins with alumina-supported iron catalysts. *React. Kinet. Catal. Lett.* **15**, 153–158 (1980).
- Xu, Y. et al. A hydrophobic FeMn@Si catalyst increases olefins from syngas by suppressing C<sub>1</sub> by-products. *Science* **371**, 610–613 (2021).
- Wang, P. et al. Synthesis of stable and low-CO<sub>2</sub> selective  $\epsilon$ -iron carbide Fischer-Tropsch catalysts. *Sci. Adv.* **4**, eaau2947 (2018).
- de Smit, E. et al. Stability and reactivity of  $\epsilon$ - $\chi$ - $\theta$  iron carbide catalyst phases in Fischer-Tropsch synthesis: controlling  $\mu$ . *J. Am. Chem. Soc.* **132**, 14928–14941 (2010).
- Chen, J. G. Carbide and nitride overlayers on early transition metal surfaces: preparation, characterization, and reactivities. *Chem. Rev.* **96**, 1477–1498 (1996).
- Zhong, L. et al. Cobalt carbide nanoparticles for direct production of lower olefins from syngas. *Nature* **538**, 84–87 (2016).
- Xie, J. et al. Promoted cobalt metal catalysts suitable for the production of lower olefins from natural gas. *Nat. Commun.* **10**, 167 (2019).
- Ma, W. et al. Quantitative comparison of iron and cobalt based catalysts for the Fischer-Tropsch synthesis under clean and poisoning conditions. *Catal. Today* **343**, 125–136 (2020).
- Davis, B. H. Fischer-Tropsch synthesis: comparison of performances of iron and cobalt catalysts. *Ind. Eng. Chem. Res.* **46**, 8938–8945 (2007).
- Broos, R. J. P. *Computational Modelling of the Fischer-Tropsch Reaction on Iron Carbides*. PhD thesis, TU Eindhoven (2020).
- Santos, V. P. et al. Metal organic framework-mediated synthesis of highly active and stable Fischer-Tropsch catalysts. *Nat. Commun.* **6**, 6451 (2015).
- Liu, J.-X., Wang, P., Xu, W. & Hensen, E. J. M. Particle size and crystal phase effects in Fischer-Tropsch catalysts. *Engineering* **3**, 467–476 (2017).
- Dinse, A., Aigner, M., Ulbrich, M., Johnson, G. R. & Bell, A. T. Effects of Mn promotion on the activity and selectivity of Co/SiO<sub>2</sub> for Fischer-Tropsch synthesis. *J. Catal.* **288**, 104–114 (2012).
- Ma, W. et al. Fischer-Tropsch synthesis: influence of CO conversion on selectivities, H<sub>2</sub>/CO usage ratios, and catalyst stability for a Ru promoted Co/Al<sub>2</sub>O<sub>3</sub> catalyst using a slurry phase reactor. *Top. Catal.* **54**, 757 (2011).
- O'Brien, R. J. & Davis, B. H. Impact of copper on an alkali promoted iron Fischer-Tropsch catalyst. *Catal. Lett.* **94**, 1–6 (2004).
- Shi, B., O'Brien, R. J., Bao, S. & Davis, B. H. Mechanism of the isomerization of 1-alkene during iron-catalyzed Fischer-Tropsch synthesis. *J. Catal.* **199**, 202–208 (2001).
- Schulz, H. & Claeys, M. Reactions of  $\alpha$ -olefins of different chain length added during Fischer-Tropsch synthesis on a cobalt catalyst in a slurry reactor. *Appl. Catal. A* **186**, 71–90 (1999).
- Li, H. et al. Effect of reaction temperature and H<sub>2</sub>/CO ratio on deactivation behavior of precipitated iron Fischer-Tropsch synthesis catalyst. *Catal. Today* **405–406**, 277–284 (2022).
- Yang, C., Zhao, H., Hou, Y. & Ma, D. Fe<sub>5</sub>C<sub>2</sub> nanoparticles: a facile bromide-induced synthesis and as an active phase for Fischer-Tropsch synthesis. *J. Am. Chem. Soc.* **134**, 15814–15821 (2012).
- Zhao, H. et al. Atomic-scale structure dynamics of nanocrystals revealed by in situ and environmental transmission electron microscopy. *Adv. Mater.* **35**, 2206911 (2023).
- Tucker, C. L. et al. Manganese promotion of a cobalt Fischer-Tropsch catalyst to improve operation at high conversion. *J. Catal.* **411**, 97–108 (2022).
- Claeys, M. et al. Oxidation of Hägg carbide during high-temperature Fischer-Tropsch synthesis: size-dependent thermodynamics and in situ observations. *ACS Catal.* **11**, 13866–13879 (2021).

**Publisher's note** Springer Nature remains neutral with regard to jurisdictional claims in published maps and institutional affiliations.



**Open Access** This article is licensed under a Creative Commons Attribution 4.0 International License, which permits use, sharing, adaptation, distribution and reproduction in any medium or format, as long as you give appropriate credit to the original author(s) and the source, provide a link to the Creative Commons licence, and indicate if changes were made. The images or other third party material in this article are included in the article's Creative Commons licence, unless indicated otherwise in a credit line to the material. If material is not included in the article's Creative Commons licence and your intended use is not permitted by statutory regulation or exceeds the permitted use, you will need to obtain permission directly from the copyright holder. To view a copy of this licence, visit <http://creativecommons.org/licenses/by/4.0/>.

© The Author(s) 2024

## Methods

## Materials

**Raney iron precursor.** Iron-aluminium alloy powder (50:50 by weight, Sigma-Aldrich) was added into an 8 mol l<sup>-1</sup> KOH (AR, Sinopharm Chemical Reagent) solution in a flask under stirring and heated to 70 °C to dissolve the aluminium in the alloy<sup>36,37</sup>. Afterwards, K<sup>+</sup> and AlO<sub>2</sub><sup>-</sup> ions were removed by washing with deionized water (ten times) and ethanol (seven times). The iron powder sample was transferred by means of a sealable quartz tube into a glove box and subsequently dried in an argon flow at room temperature for 6 h. The resulting porous iron powder was kept in a container with a seal in a glove box. Before loading the sample in appropriate in situ cells (XRD and Mössbauer spectroscopy characterization) or a stainless-steel reactor for FT activity measurements, the sample was passivated in a flow of 1% O<sub>2</sub> in helium at room temperature for 20 h.

**Manganese-Raney iron precursor.** Manganese (0.5–12.5 wt%) was added to the Raney iron precursor (directly after removal of aluminium) by wet impregnation using a Mn(NO<sub>3</sub>)<sub>2</sub> solution. The sample was then dried in a vacuum oven at room temperature for 12 h.

**Potassium-Raney iron precursor (Extended Data Fig. 3c).** Potassium (1 wt%) was added to the Raney iron precursor (directly after removal of aluminium) by wet impregnation using a KNO<sub>3</sub> solution. The sample was then dried in a vacuum oven at room temperature for 12 h.

## Characterization

In situ X-ray diffraction (in situ XRD) was carried out on a Rigaku D/max-2600/PC instrument equipped with a D/teX ultrahigh-speed detector and scintillation counter. The X-ray generator consisted of a copper rotating anode with a maximum power of 9 kW. All measurements were carried out at 40 mA and 40 kV. In situ XRD patterns were recorded in an Anton Par XRK-900 cell equipped with a CO/H<sub>2</sub>/Ar gas inlet system.

Environmental TEM (ETEM) images were recorded in an aberration-corrected FEI Titan ETEM G2 instrument at an acceleration voltage of 300 kV (ref. 38). Syngas was introduced for 1 h under 1,200 Pa at 320 °C as a pretreatment. The carburization temperature was then raised to 350 °C in about 0.5 h, followed by monitoring the sample continuously.

In situ Mössbauer spectroscopy was carried out in an in situ high-pressure cell suitable for Mössbauer spectroscopy<sup>39</sup>. Transmission <sup>57</sup>Fe Mössbauer spectra were collected at -153 °C with a sinusoidal velocity spectrometer using a <sup>57</sup>Co(Rh) source. The source and the sample were kept at the same temperature during the measurements. Mosswin 4.0 software was used for spectra fitting<sup>40</sup>.

## Catalytic activity measurements

**In situ carburization of  $\chi$ -Fe<sub>5</sub>C<sub>2</sub> and Mn- $\chi$ -Fe<sub>5</sub>C<sub>2</sub> and FT/LAO catalytic activity measurements.** A 75 mg amount of Raney iron precursor or manganese/Raney iron precursor, the latter also containing 75 mg of Raney iron, was diluted with 1,500 mg silicon carbide and loaded into a stainless-steel tubular fixed-bed reactor with an external diameter of 14.5 mm, internal diameter of 9 mm, length of 305 mm and total internal volume of 20 ml. An exception was the test in Table 1, row 1, for which 225 mg Raney iron of a manganese-Raney iron precursor was diluted with 4,500 mg silicon carbide to achieve a low SV of 5,000 ml g<sub>cat</sub><sup>-1</sup> h<sup>-1</sup>. The catalyst precursor was in situ carburized in a syngas flow (H<sub>2</sub>/CO/He = 100/3.2/21.8) while increasing the temperature to 350 °C at a rate of 1 °C min<sup>-1</sup>, followed by a dwell of 6 h at ambient pressure and an SV of 75,000 ml g<sub>cat</sub><sup>-1</sup> h<sup>-1</sup>. After cooling the reactor to 250 °C (240 °C for the test in Table 1, row 3), the reactor feed was switched to the feed mixture and the reactor pressure was increased to the desired value. The start of the reaction was defined as the time at which these

conditions were reached. The reactor was then ramped to the indicated temperature.

For the comparison between  $\chi$ -Fe<sub>5</sub>C<sub>2</sub> and Mn- $\chi$ -Fe<sub>5</sub>C<sub>2</sub> (Table 1, rows 1 and 2), the reaction conditions were as follows: a feed mixture SV of H<sub>2</sub>/CO/He = 12,000/8,000/8,000 ml g<sub>cat</sub><sup>-1</sup> h<sup>-1</sup>, a reaction pressure of 2.3 MPa and a reaction temperature of 250 °C. For the evaluation of the Mn- $\chi$ -Fe<sub>5</sub>C<sub>2</sub> catalyst under different temperatures and pressures (Fig. 1a–f and rows 3–6 of Table 1), the reaction conditions were as follows: a feed mixture of H<sub>2</sub>/CO/Ar (internal standard) = 1.5/0.95/0.05 at a total SV of 5,000, 30,000 or 60,000 ml g<sub>cat</sub><sup>-1</sup> h<sup>-1</sup>, a reaction pressure of either 2.5 or 3.0 MPa and a reaction temperature of 250, 290 or 320 °C (heating rate 0.1 °C min<sup>-1</sup>). For the evaluation of the Mn- $\chi$ -Fe<sub>5</sub>C<sub>2</sub> catalyst in Extended Data Table 2, the reaction conditions were as follows: a feed mixture SV of H<sub>2</sub>/CO = 1.5 at a total SV of 30,000, 60,000, 75,000 or 90,000 ml g<sub>cat</sub><sup>-1</sup> h<sup>-1</sup> with no inert gas added, a reaction pressure of 2.5 MPa and a reaction temperature of 250, 270, 290 or 310 °C (heating rate 0.1 °C min<sup>-1</sup>). For the evaluation of Mn- $\chi$ -Fe<sub>5</sub>C<sub>2</sub> (Extended Data Fig. 5a) and K- $\chi$ -Fe<sub>5</sub>C<sub>2</sub> (Extended Data Fig. 3c), the reaction conditions were as follows: a feed mixture SV of H<sub>2</sub>/CO/He = 36,000/24,000/24,000 ml g<sub>cat</sub><sup>-1</sup> h<sup>-1</sup> or 72,000/48,000/48,000 ml g<sub>cat</sub><sup>-1</sup> h<sup>-1</sup> and a reaction pressure at 2.3 MPa. The reaction temperature was 315 or 325 °C for these measurements (heating rate 0.5 °C min<sup>-1</sup>). For the long-term test for Mn- $\chi$ -Fe<sub>5</sub>C<sub>2</sub> (Extended Data Fig. 5c), the reaction conditions were as follows: a feed mixture SV of H<sub>2</sub>/CO/He = 60,000/40,000/40,000 ml g<sub>cat</sub><sup>-1</sup> h<sup>-1</sup> and a reaction pressure at 2.3 MPa. We used a low ramp rate of 2 °C h<sup>-1</sup> to avoid overheating issues due to the exothermicity of the reaction. Therefore, it took 35 h to raise the temperature from 250 °C to 320 °C.

The effluent gas flow was analysed by an online Agilent 7890 gas chromatograph equipped with two thermal conductivity detectors and one flame ionization detector. Each result was acquired from a single experiment. All of the SVs are calculated on the basis of the weight of the Raney iron catalyst precursor without a promoter or silicon carbide diluent.

The CO conversion and product selectivity were calculated as below.

The CO conversion ( $X_{CO}$ ) was calculated by

$$X_{CO} = \frac{CO_{inlet} - CO_{outlet}}{CO_{inlet}} \times 100\% \quad (1)$$

The CO<sub>2</sub> selectivity ( $S_{CO_2}$ ) was calculated by

$$S_{CO_2} = \frac{CO_{2,outlet}}{CO_{inlet} - CO_{outlet}} \times 100\% \quad (2)$$

The carbon-based hydrocarbon selectivity ( $S_{C_xH_y}$ ) was calculated by

$$S_{C_xH_y} = \frac{x C_x H_y_{outlet}}{CO_{inlet} - CO_{outlet}} \times 100\% \quad (3)$$

The indicated parameters represent the inlet and outlet molar flows determined.

The CO catalyst time yield (CTY<sub>CO</sub>) was calculated by

$$CTY_{CO} = \frac{X_{CO} \times CO_{inlet}}{22,400 \text{ (ml mol}^{-1}) \times 3,600 \text{ (s h}^{-1})} \quad (4)$$

The carbon-based hydrocarbon catalyst time yield (CTY<sub>C<sub>x</sub>H<sub>y</sub></sub>) was calculated by

$$CTY_{C_xH_y} = CTY_{CO} \times S_{C_xH_y} \quad (5)$$

The experimental chain-growth probability was calculated by the ASF distribution as follows



$$\ln\left(\frac{W_n}{n}\right) = n \ln \alpha + \ln[(1 - \alpha)^2 / \alpha] \quad (6)$$

in which  $n$  is the number of carbon atoms in a particular hydrocarbon product,  $W_n$  is the weight fraction of a product with  $n$  number of carbon atoms and  $\alpha$  is the chain-growth probability.

### Theoretical modelling

**Density functional theory calculations.** Density functional theory (DFT) calculations were carried out to obtain the energetics for elementary reaction steps relevant to the FT reaction on  $\chi$ -Fe<sub>3</sub>C<sub>2</sub>. All spin-polarized DFT calculations were conducted using the projector augmented-wave method and the Perdew–Burke–Ernzerhof functional, as implemented in the Vienna ab initio simulation package code. Solutions of the Kohn–Sham equations were obtained using a basis set of plane waves with a cutoff energy of 400 eV. Sampling of the Brillouin zone was carried out using a  $5 \times 5 \times 1$   $k$ -point mesh. Higher cutoff energies or a finer Brillouin zone sampling did not lead to substantial energy differences. All atoms were allowed to relax during the optimization of the empty surfaces. We used a  $2 \times 2 \times 1$  unit cell for the (100) surface, containing 80 iron and 32 carbon atoms, with a layer thickness of 10.31 Å. A vacuum layer of 15 Å was added perpendicular to the surface to avoid spurious interactions between neighbouring images. Adsorption of atoms and molecules was carried out on the top side of the slab, whereas the lower half was frozen. A dipole correction was carried out for all adsorbed states. Further technical details such as Vienna ab initio simulation package settings for these iron carbide calculations are described elsewhere<sup>23</sup>. The adsorption energies of the gas-phase molecules were determined by subtracting the energies of the empty surface and the free adsorbate from the adsorbed state. The energy of the adsorbate in the gas phase was obtained by placing a molecule at the centre of a  $10 \times 10 \times 10$  Å<sup>3</sup> unit cell, using the  $\Gamma$ -point for  $k$ -point sampling. Transition states were acquired using the nudged elastic band method<sup>41</sup>. A frequency analysis was carried out to confirm that all transition geometries correspond to a first-order saddle point on the potential energy surface with an imaginary frequency in the direction of the reaction coordinate. The corresponding normal-mode vibrations were also used to calculate the zero-point energy correction. We also corrected the barriers for the migration of fragments after dissociation by considering the energy difference of the geometry directly after dissociation and their most stable adsorption positions at infinite distance.

We carried out DFT calculations to determine the energetics of elementary reaction steps of the conversion of synthesis gas into hydrocarbons (methane, olefins and paraffins) and CO<sub>2</sub> and H<sub>2</sub>O. The energy barriers and their corresponding pre-exponential factors are listed in Extended Data Table 1. The (100) surface of  $\chi$ -Fe<sub>3</sub>C<sub>2</sub> was selected, because this surface is a stable surface termination of Hägg carbide and also allows for facile C–O bond dissociation, which is an essential step in the FT reaction<sup>42</sup>. Extended Data Table 1 shows forward and backward activation energies and the corresponding pre-exponential factors for the consecutive hydrogenation steps of adsorbed carbon to methane and the removal of oxygen as H<sub>2</sub>O and CO<sub>2</sub>. Extended Data Table 1 shows forward and backward activation energies and the corresponding pre-exponential factors for the C–C coupling reactions and the hydrogenation to ethylene and ethane.

**Microkinetics modelling.** For the construction of the microkinetic model of the FT reaction, differential equations for all reaction intermediates on the catalytic surface were constructed using the rate constants of all considered elementary reaction steps. Herein, we assumed that all adsorbates occupy one active site. For adsorption, we assumed that the adsorbate loses one translational degree of freedom in the transition state with respect to the initial state. For desorption, we assumed that the species gains two translational degrees of freedom and three rotational degrees of freedom in the transition state with respect to

the initial state. From these two assumptions, the rate of adsorption and desorption are as follows:

$$k_{\text{ads}} = \frac{P \times A}{\sqrt{2\pi \times m \times k_B \times T}} \quad (7)$$

$$k_{\text{des}} = \frac{k_B \times T^3}{h^3} \times \frac{A \times (2\pi \times m \times k_B)}{\sigma \theta_{\text{rot}}} \times \frac{E_{\text{des}}}{e^{RT}} \quad (8)$$

Herein,  $k_{\text{ads}}$  is the rate constant for the adsorption of the adsorbate,  $P$  is the pressure in pascals,  $A$  is surface area in square metres,  $m$  is the mass of the reactant in kilograms,  $k_B$  is the Boltzmann constant in joules per kelvin,  $T$  is the temperature in kelvin,  $k_{\text{des}}$  is the rate constant for the desorption of the adsorbate,  $h$  is the Planck constant in joules multiplied by seconds,  $\sigma$  is the symmetry number,  $\theta_{\text{rot}}$  the rotational temperature in kelvin,  $E_{\text{des}}$  is the desorption energy in joules per mole, and  $R$  is the gas constant in joules per kelvin per mole.

The rate constant ( $k$ ) of an elementary reaction step was determined using the Eyring equation, which is defined as follows:

$$k = \nu \exp\left(\frac{-E_{\text{act}}}{k_B T}\right) \quad (9)$$

in which  $E_{\text{act}}$  is activation energy in joules per mole,  $k_B$  the Boltzmann constant,  $T$  the temperature in kelvin, and  $\nu$  the pre-exponential factor in the unit of per second. Pre-exponential factors for the forward and backward reactions can be obtained using:

$$\nu_{\text{forward}} = \frac{k_B T}{h} \left( \frac{q_{\text{vib}}^{\text{TS}}}{q_{\text{vib}}^{\text{IS}}} \right) \quad (10)$$

and

$$\nu_{\text{backward}} = \frac{k_B T}{h} \left( \frac{q_{\text{vib}}^{\text{TS}}}{q_{\text{vib}}^{\text{FS}}} \right) \quad (11)$$

in which  $\nu_{\text{forward}}$  and  $\nu_{\text{backward}}$  refer to the pre-exponential factors for the forward and the backward reaction, respectively,  $q_{\text{vib}}$  is the vibrational partition function of the initial state (IS) and the transition state (TS), and  $h$  is Planck's constant.

All microkinetic simulations were carried out using the MKMCXX software suite<sup>43</sup>. The set of differential equations were time-integrated using the backward differentiation formula method until a steady-state solution was obtained. From the steady-state coverages, the rates of the individual elementary reactions steps were obtained using a flux analysis, as implemented in the MKMCXX software. To mimic experimental conditions, the pressure was set to 0.1 MPa over a temperature range between 510 K and 545 K. We adopted a continuously stirred tank reactor with ideal mixing using an SV chosen to obtain differential conditions over the whole temperature range. The H<sub>2</sub>/CO ratio was kept constant at 2:1. Chain growth was considered by involving coupling of two CH<sub>*x*</sub> adsorbates. Chain growth for hydrocarbon chains up to 20 carbon atoms was considered by treating the growing chain as CR, in which R = alkyl chain and considering that barriers for chain growth are independent of chain length. Adsorption energies of C<sub>2</sub> and C<sub>3</sub> intermediates were taken into account explicitly, whereas those of hydrocarbon fragments with more than three carbon atoms were taken to be equal to those of C<sub>3</sub> intermediates. Proper entropy corrections were made depending on the chain length of the hydrocarbons.

The chain-growth probability was determined from the ASF distribution by considering hydrocarbon products containing 1–20 carbon atoms:

$$\alpha = \frac{r_p}{r_p + r_t} \cong \exp\left(\frac{d \ln F_{C_n}^{\text{out}}}{dn}\right) \quad (12)$$

Herein, the chain-growth probability is defined as the rate of propagation ( $r_p$ ) over the sum of the rates of propagation and termination ( $r_t$ ).  $F_{C_n}^{\text{out}}$  corresponds to the flow rate of  $C_n$  in the experiment. This involved simulating the corresponding chain-growth probability ( $\alpha$ ) and  $C_2$  selectivity within the ASF distribution shown in Extended Data Fig. 2.

**Results of microkinetic simulations.** Extended Data Fig. 1a shows the CO conversion rate and formation rates of  $\text{CH}_4$  ( $C_1$ ) and longer hydrocarbons ( $C_2$ ) for the (100) surface of  $\chi\text{-Fe}_5\text{C}_2$  as a function of temperature. As expected, the rates exponentially increase with temperature owing to the Arrhenius dependence of the reaction rate constants. The CO conversion rate is in the same range as experimentally observed for iron carbide catalysts<sup>42,44</sup>. The selectivity towards  $\text{CH}_4$  is lower than the total selectivity towards other hydrocarbons, which is important because  $\text{CH}_4$  has a much lower value than higher hydrocarbons. Extended Data Fig. 2a shows the hydrocarbon product distribution, which indicates that, except for  $C_1$  and  $C_2$ , the longer hydrocarbons are statistically distributed according to the ASF theory. The parameter describing this distribution is the chain-growth probability and its temperature dependence is shown in Extended Data Fig. 2b. This parameter reflects the statistical nature of the growth process in which hydrocarbons can either grow by addition of a  $C_1$  monomer or desorb as a product. The decrease with temperature shows that termination as products has a higher overall activation energy than chain growth. The value of about 0.5 is slightly lower than experimentally observed in our study. Extended Data Fig. 2c shows the simulated O/P ratio to be around 3.0 with a minor dependence on temperature. These data show that both olefins and paraffins are formed as primary products. The O/P values are in the same range as experimentally observed, namely about 1.5 for the unpromoted catalyst and about 3.6 for the manganese-promoted catalyst. Extended Data Fig. 1b demonstrates that oxygen atoms originating from CO dissociation are predominantly removed as  $\text{H}_2\text{O}$ , instead of  $\text{CO}_2$ . These findings provide an explanation for the low  $\text{CO}_2$  selectivity observed in our experimental study in which a pure  $\chi\text{-Fe}_5\text{C}_2$  catalyst was used. In other studies in which the catalyst precursor is not completely converted to  $\chi\text{-Fe}_5\text{C}_2$ , competing phases often include iron oxides, which are known as good catalysts for the (reverse) water–gas shift reaction.

The computational predictions in Extended Data Table 1 show that, on  $\chi\text{-Fe}_5\text{C}_2$ , the overall barrier for  $\text{H}_2\text{O}$  formation ( $155 \text{ kJ mol}^{-1}$ ) is lower than the barrier for  $\text{CO}_2$  formation ( $181 \text{ kJ mol}^{-1}$ ). This implies that  $\text{H}_2\text{O}$  formation is preferred on  $\chi\text{-Fe}_5\text{C}_2$  over  $\text{CO}_2$  formation as the oxygen removal step. To verify this prediction based on the overall energy barrier under reaction conditions, we used microkinetic simulations based on DFT-based reaction energetics and found that oxygen removal reactions proceed primarily through the formation of  $\text{H}_2\text{O}$  (99.4% at 525 K) instead of  $\text{CO}_2$  (0.6% at 525 K; Extended Data Fig. 1c). These simulations showing a very low  $\text{CO}_2$  selectivity pertain to the zero-conversion limit and, thus, represent so-called primary  $\text{CO}_2$  production. The microkinetic simulations also provide a deeper insight into the reaction mechanism including the interplay between the surface intermediates. In Extended Data Fig. 1d we show that, in addition to CO dissociation, oxygen removal and carbon hydrogenation (as part of the chain-growth mechanism) control the overall reaction rate. These findings are in keeping with the periodic trends predicted in previous work<sup>43</sup>.

**Rietveld refinement XRD patterns.** The results of Rietveld refinement of the XRD patterns using the Fullprof software are shown in Extended Data Fig. 7g. Rietveld refinement confirmed the phase purity of  $\chi\text{-Fe}_5\text{C}_2$  (no substantial contribution of other phases) with a goodness of fit of

$\chi^2 = 7.58\%$ ,  $R_p = 18.7\%$ ,  $R_{wp} = 15.3\%$  and  $R_{exp} = 5.6\%$ . The space group and lattice parameters listed in Extended Data Fig. 7g are in good agreement with published data for  $\chi\text{-Fe}_5\text{C}_2$  (ref. 45). The atomic positions of the specific sites for the  $\chi\text{-Fe}_5\text{C}_2$  structure are listed in Extended Data Fig. 7h. Note that the data were acquired in an in situ XRD reaction chamber under a nitrogen flow after obtaining the  $\chi\text{-Fe}_5\text{C}_2$  particles through the described synthesis method.

## Data availability

All data are available in the main text or the Supplementary Information and are also available from the corresponding authors on reasonable request.

- Chen, K. R., Hanson, F. V., Nag, N. & Oblad, A. G. In *ACS Symposium on Syngas Conversion Catalysis Advances in Gasification* 95–108 (1986).
- Sun, B. et al. A highly selective Raney Fe@HZSM-5 Fischer–Tropsch synthesis catalyst for gasoline production: one-pot synthesis and unexpected effect of zeolites. *Catal. Sci. Technol.* **2**, 1625 (2012).
- Wang, R. The dynamics of the peel. *Nat. Catal.* **3**, 333–334 (2020).
- Wezendonk, T. A. et al. Elucidating the nature of Fe species during pyrolysis of the Fe-BTC MOF into highly active and stable Fischer–Tropsch catalysts. *ACS Catal.* **6**, 3236–3247 (2016).
- Klencsar, Z. Mössbauer spectrum analysis by evolution algorithm. *Nucl. Instrum. Methods Phys. Res. B* **129**, 527–533 (1997).
- Henkelman, G. & Jónsson, H. Improved tangent estimate in the nudged elastic band method for finding minimum energy paths and saddle points. *J. Chem. Phys.* **113**, 9978–9985 (2000).
- Pour, A. N., Shahri, S. M. K., Zamani, Y., Irani, M. & Tehrani, S. Deactivation studies of bifunctional Fe-HZSM5 catalyst in Fischer–Tropsch process. *J. Nat. Gas Chem.* **17**, 242–248 (2008).
- Filot, I. A., van Santen, R. A. & Hensen, E. J. The optimally performing Fischer–Tropsch catalyst. *Angew. Chem. Int. Ed.* **53**, 12746–12750 (2014).
- Chang, Q. et al. Relationship between iron carbide phases ( $\epsilon\text{-Fe}_2\text{C}$ ,  $\text{Fe}_3\text{C}_2$ , and  $\chi\text{-Fe}_5\text{C}_2$ ) and catalytic performances of Fe/SiO<sub>2</sub> Fischer–Tropsch catalysts. *ACS Catal.* **8**, 3304–3316 (2018).
- Retief, J. J. Powder diffraction data and Rietveld refinement of Hägg-carbide,  $\chi\text{-Fe}_5\text{C}_2$ . *Powder Diffr.* **14**, 130–132 (1999).

**Acknowledgements** We acknowledge X. Ma for inspiration and guidance on this work; X. Meng, T. Wang, X. Zhang, J. Jiang, W. Li, Y. Li and L. Ma for help with catalyst preparation, catalytic tests, data analysis and in situ XRD measurements; and R. Pestman, X. Ren, S. Li and T. F. Kimpel for help with the catalytic performance measurements and discussions on the mechanism. This work was supported by the National Key Research and Development Program of China (number 2022YFB4101400) and the CHN Energy Science and Technology innovation project (numbers GJPT-23-18 and GJNY-21-72). E.J.M.H. received financial support through an NWO-Top grant awarded by the Netherlands Organization for Scientific Research. This work was partly supported by the Netherlands Center for Multiscale Catalytic Energy Conversion, an NWO Gravitation programme funded by the Ministry of Education, Culture and Science of the government of the Netherlands. The ETEM experiments were supported by the Natural Science Foundation of China (number 12034002). Open access funding was provided by the National Institute of Clean-and-Low-Carbon Energy.

**Author contributions** P.W. designed and carried out FTLAO catalyst synthesis, characterization, catalytic tests and data analysis, and drafted the manuscript; F.-K.C., Y.S. and R.W. contributed to ETEM experimental design, operation and data analysis; J.C. and W.C. carried out catalyst kinetic testing and contributed to characterization, catalytic tests, data analysis and discussion; A.I.D. contributed to high-pressure in situ Mössbauer spectroscopy experimental design, operation and data analysis; J.D. contributed to paper background and structure drafting, and all of the techno-economic data collection, treatment and data analysis; R.J.P.B. contributed to computational modelling; B.F. contributed to in situ XRD operation; Y.L. and Q.L. contributed to discussion on the catalyst; Z.M. guided the discussion on the industrial process and energy strategy; E.J.M.H. contributed to the design of the work, guided the writing of the paper, and contributed to all tests and data analysis and discussion. All of the authors contributed to the discussion of the results and commented on the manuscript.

**Competing interests** The authors declare no competing interests.

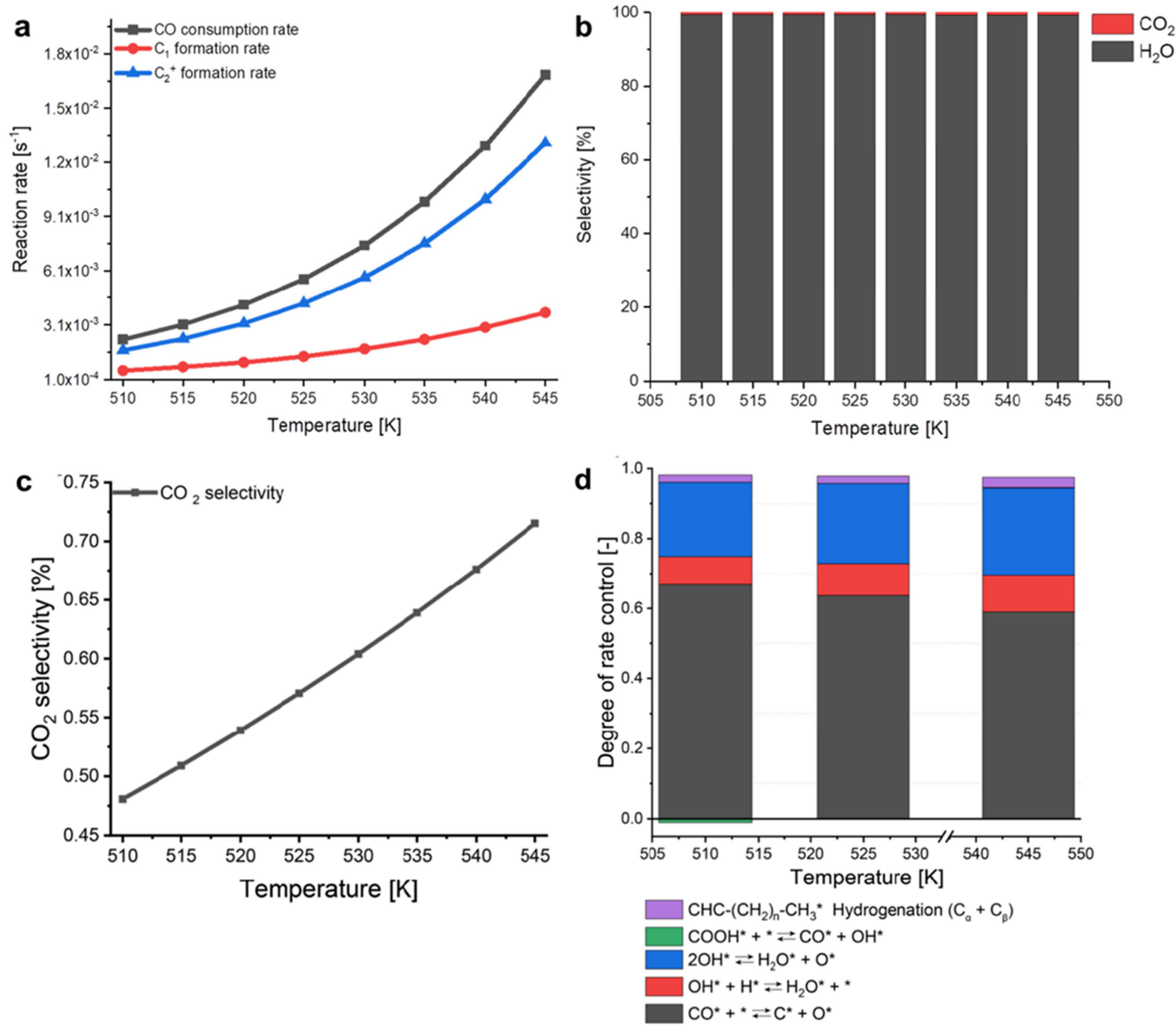
## Additional information

**Supplementary information** The online version contains supplementary material available at <https://doi.org/10.1038/s41586-024-08078-5>.

**Correspondence and requests for materials** should be addressed to Peng Wang, Zhuowu Men or Emiel J. M. Hensen.

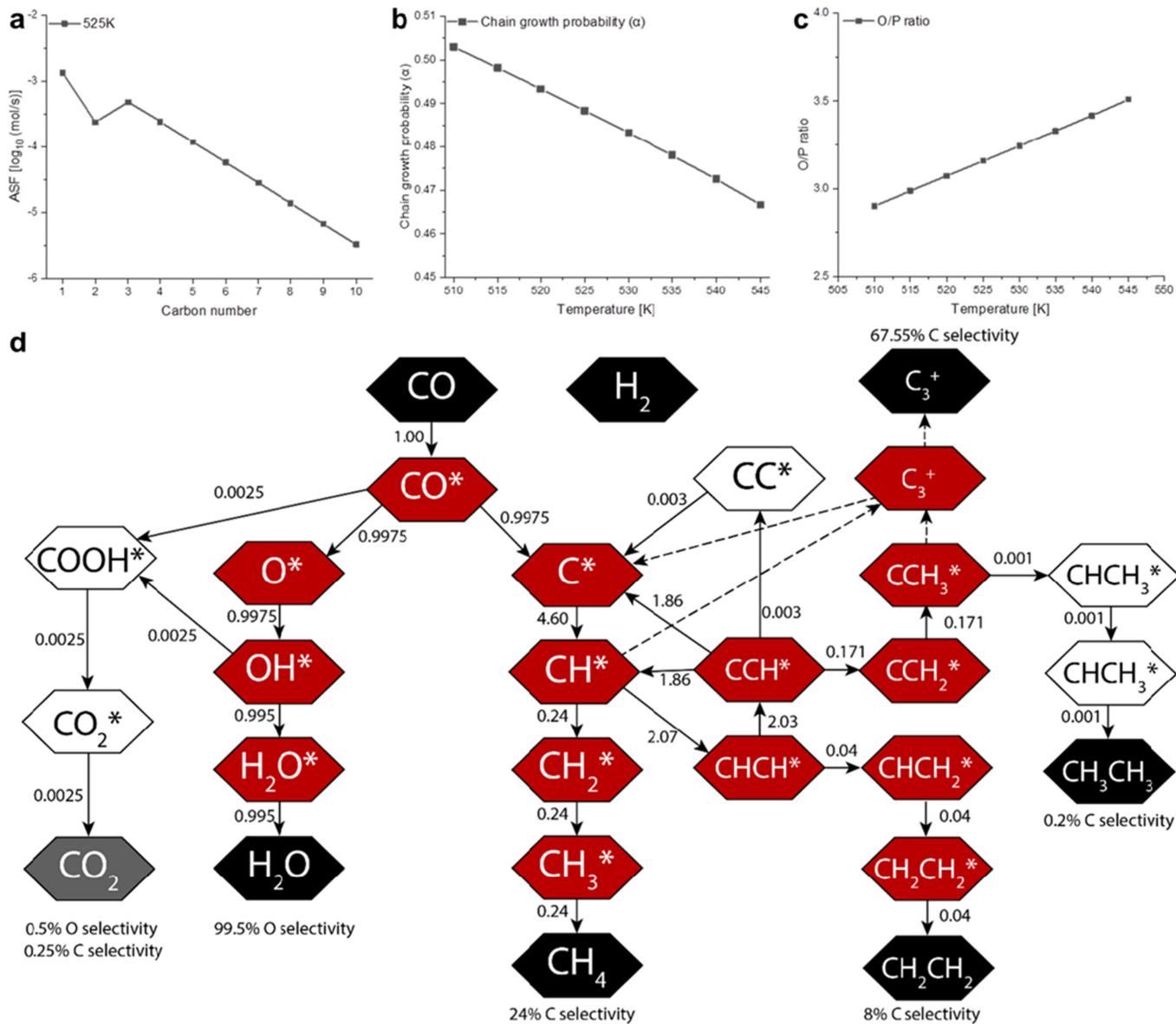
**Peer review information** Nature thanks Olumide Ayodele, Michael Claeys, Muthu Kumaran Gnanamani, Jia Yang and the other, anonymous, reviewer(s) for their contribution to the peer review of this work.

**Reprints and permissions information** is available at <http://www.nature.com/reprints>.



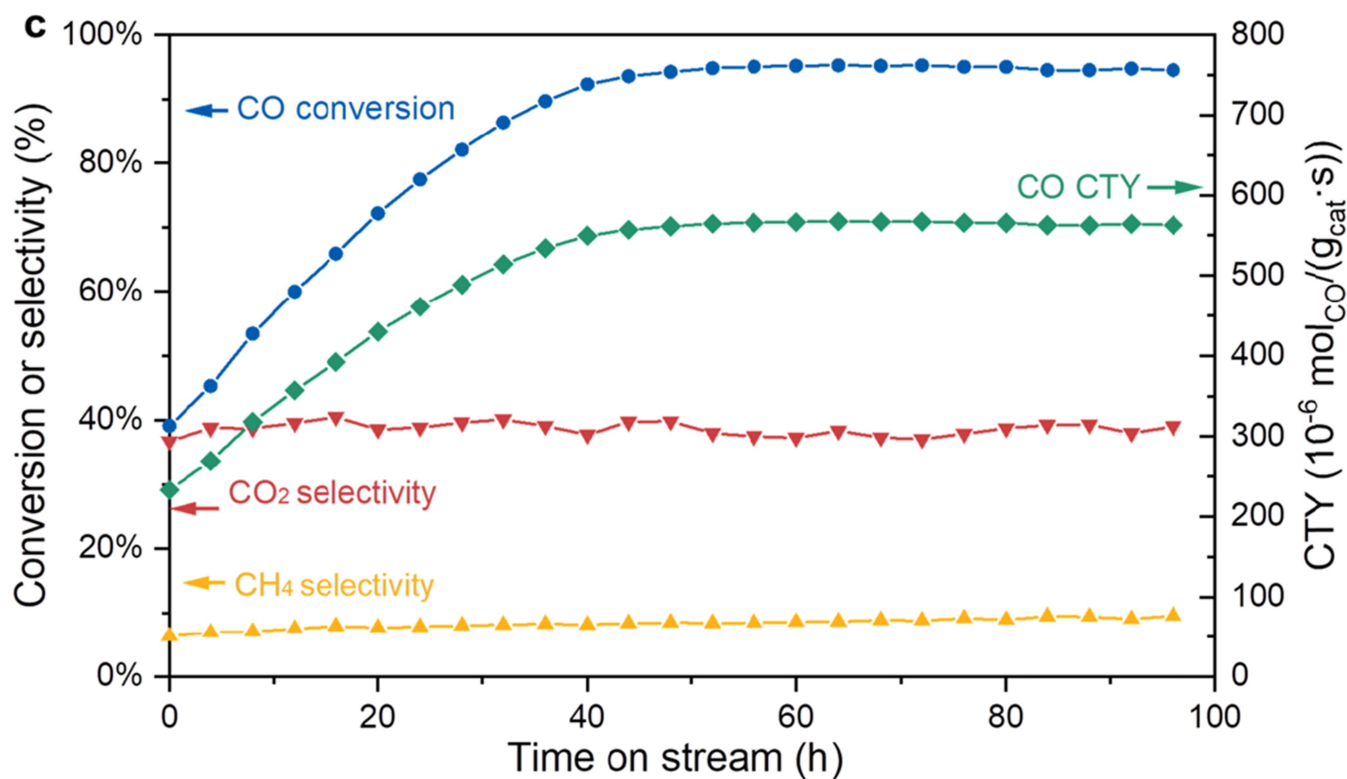
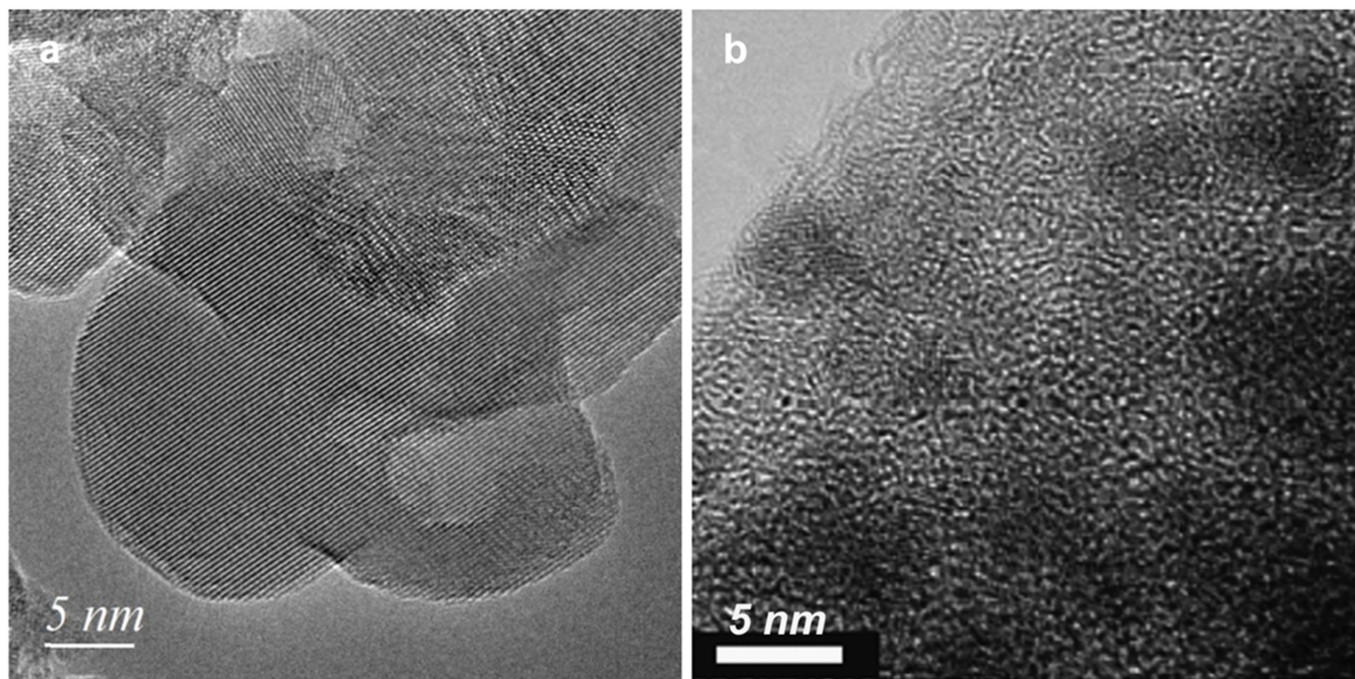
**Extended Data Fig. 1 | Microkinetics simulations for  $\chi$ -Fe<sub>3</sub>C<sub>2</sub>-(100) surface.** (a) CO consumption (grey), C<sub>1</sub> formation (red), and C<sub>2</sub><sup>+</sup> formation (blue) rates as a function of the reaction temperature (0.1 MPa, H<sub>2</sub>/CO = 2). Rates are determined by microkinetics simulations based on DFT-computed reaction energetics. (b) Selectivity towards H<sub>2</sub>O and CO<sub>2</sub> as a function of the reaction

temperature (0.1 MPa, H<sub>2</sub>/CO = 2). (c) CO<sub>2</sub> selectivity of the FT reaction between 510 K and 545 K at 1 bar in the zero-conversion limit. (d) Degree of rate control analysis in microkinetic simulations at 510 K, 525 K and 545 K (0.1 MPa, H<sub>2</sub>/CO = 2). Rates are determined by microkinetics simulations based on DFT-computed reaction energetics.



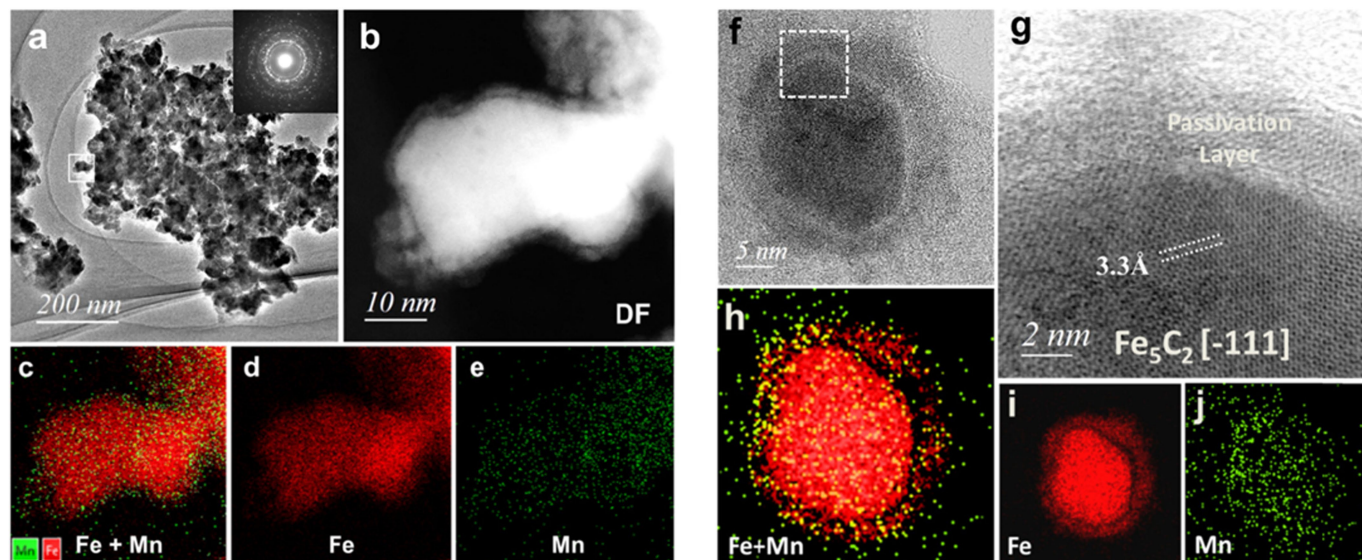
**Extended Data Fig. 2 | Microkinetics simulations of hydrocarbon products for  $\chi\text{-Fe}_3\text{C}_2(100)$  surface.** (a) Distribution of hydrocarbons obtained during microkinetics simulations of the FT reaction at 525 K. (b) the chain-growth probability  $\alpha$  and (c) the olefins-to-paraffins (O/P) ratio as a function of the reaction temperature (0.1 MPa,  $\text{H}_2/\text{CO} = 2$ ). (d) Network plot at 525 K: the net relative rates (CO conversion rate set at unity) are indicated next to the arrows. The dashed arrows indicate the routes towards  $\text{C}_3^+$  formation (0.1 MPa,  $\text{H}_2/\text{CO} = 2$ ). Red hexagons represent the major surface intermediates, black

hexagons the major gaseous components, grey hexagons the minor gaseous components, and white hexagons minor surface intermediates. Surface intermediates and products with a relative contribution less than  $10^{-4}$  were omitted. CO dissociation proceeds via direct C-O bond scission and the resulting O atom is mainly removed as  $\text{H}_2\text{O}$ . The dominant C-C coupling mechanism involves association of two CH species to produce the  $\text{C}_2$  intermediate and association of CH and CR for obtaining higher hydrocarbons.



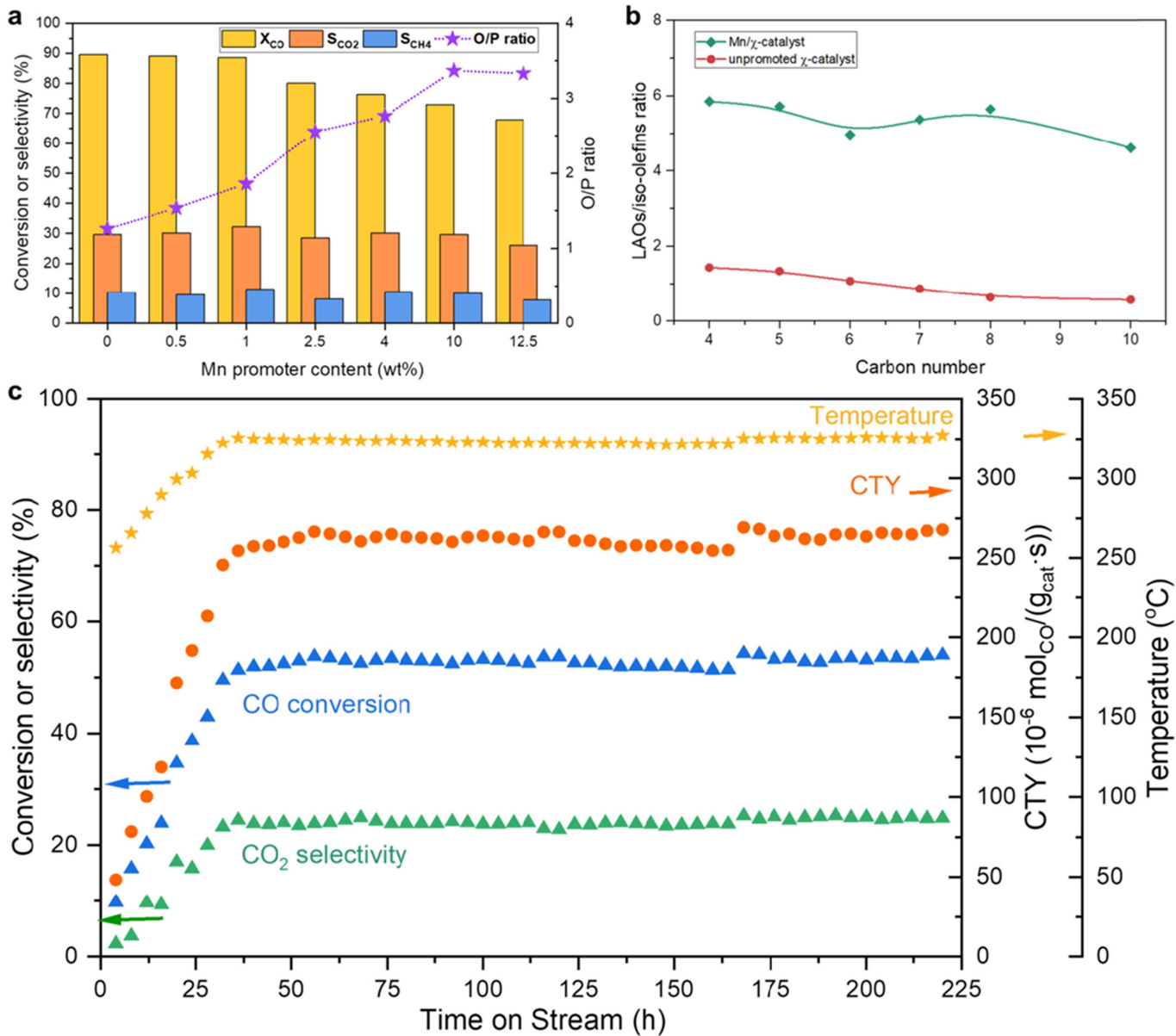
**Extended Data Fig. 3 | Comparison between phase-pure  $\chi$ -Fe-carbide and non-phase-pure  $\chi$ -Fe-carbide.** (a)-(b) Comparison representative HRTEM images: (a) phase-pure  $\chi$ -Fe-carbide in the present work and (b) non-phase-pure  $\chi$ -Fe-carbide catalyst (38-Fe@C) from reference<sup>24</sup>. (c) Catalytic performance of

1 wt% K-promoted phase-pure  $\chi$ -Fe-carbide catalyst. Reaction condition: 325 °C, 2.3 MPa,  $\text{SV}_{\text{H}_2/\text{CO}/\text{He}} = 72,000/48,000/48,000 \text{ ml}/(\text{g}_{\text{cat}} \cdot \text{h})$ . Micrograph in **b** adapted from ref. 24, Springer Nature Limited.



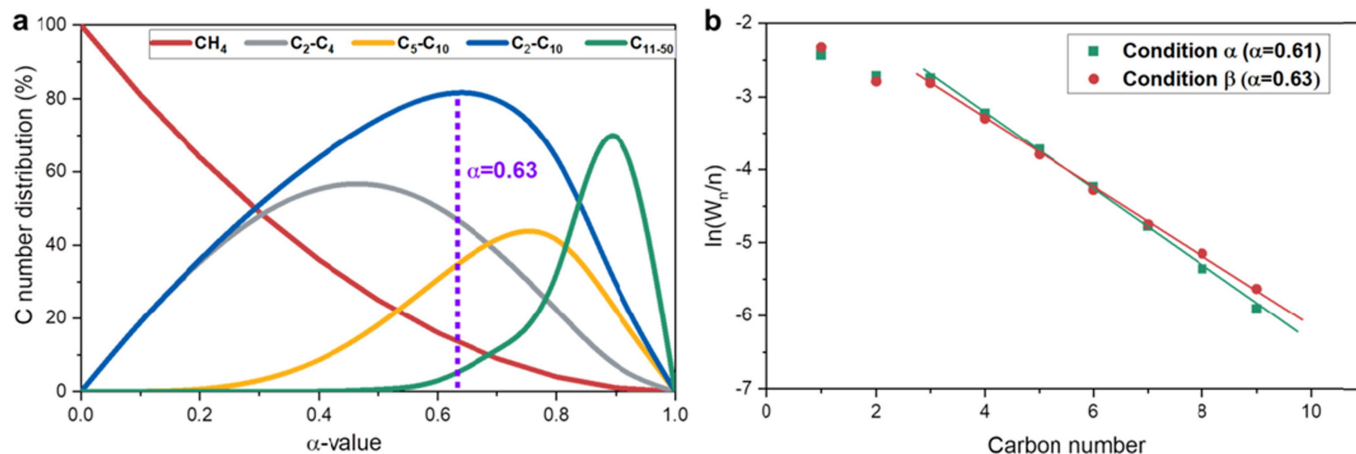
**Extended Data Fig. 4 | Ex situ TEM images of Mn- $\chi$ -Fe<sub>5</sub>C<sub>2</sub> and used Mn- $\chi$ -Fe<sub>5</sub>C<sub>2</sub>.** (a) Representative TEM image of Mn- $\chi$ -Fe<sub>5</sub>C<sub>2</sub>. The selected-area electron diffraction (SAED) pattern in the inset shows the diffraction pattern of  $\chi$ -Fe<sub>5</sub>C<sub>2</sub>. (b) Dark-field (DF) image of a single particle of  $\chi$ -Fe<sub>5</sub>C<sub>2</sub> (white-square in a) and (c)-(e) corresponding STEM-EDS images, showing the uniform distribution of Mn promoter on the  $\chi$ -Fe<sub>5</sub>C<sub>2</sub> surface. (f)-(j) Mn- $\chi$ -Fe<sub>5</sub>C<sub>2</sub> after use in the FT

reaction at 290 °C, 2.5 MPa, SV H<sub>2</sub>/CO/Ar = 18,000/11,400/600 ml/(g<sub>cat</sub>·h), 160 h. (f) Bright-field (BF) image of a single particle of  $\chi$ -Fe<sub>5</sub>C<sub>2</sub>. (g) BF image of a single  $\chi$ -Fe<sub>5</sub>C<sub>2</sub> particle (white-square in f) and (h)-(j) corresponding STEM-EDS images showing the distribution of Mn promoter on the surface of used Mn- $\chi$ -Fe<sub>5</sub>C<sub>2</sub>. The Mn promoter content is 10 wt%.



**Extended Data Fig. 5 | Catalytic activity tests for Mn-promoted FTLAG catalysts.** (a) Catalytic performance of Mn-promoted FTLAG catalysts (Mn- $\chi$ -Fe<sub>3</sub>C<sub>2</sub>). Reaction conditions: 315 °C, 2.3 MPa, SV H<sub>2</sub>/CO/He = 36,000/24,000/24,000 ml/(g<sub>cat</sub>·h). (b) LAOs to iso-olefins ratio as a function of the carbon number for Mn- $\chi$ -Fe<sub>3</sub>C<sub>2</sub> and  $\chi$ -Fe<sub>3</sub>C<sub>2</sub>. Reaction conditions: 250 °C,

2.3 MPa, SV H<sub>2</sub>/CO/He = 12,000/8,000/8,000 ml/(g<sub>cat</sub>·h). (c) Stability evaluation for the Mn- $\chi$ -Fe<sub>3</sub>C<sub>2</sub> catalyst. Reaction conditions: 320–325 °C, 2.3 MPa, SV H<sub>2</sub>/CO/He = 60,000/40,000/40,000 ml/(g<sub>cat</sub>·h). CTY means the catalyst time yield. For (b) and (c), the Mn promoter content is 4 wt%.



**Extended Data Fig. 6 | Hydrocarbon product distribution study for FT/LAO catalysts.** (a) Predicted ASF hydrocarbon product distribution as a function of the chain-growth probability ( $\alpha$ ). The  $\text{C}_2\text{-C}_{10}$  products selectivity is maximized when the  $\alpha$  value is -0.63. (b) Experimental ASF plots for  $\text{Mn-}\gamma\text{-Fe}_2\text{C}_2$  obtained under different reaction conditions.  $W_n$  is the fraction by weight of a

hydrocarbon with carbon number  $n$ . Reaction conditions: (green) 250 °C, 3.0 MPa,  $\text{SV H}_2/\text{CO}/\text{Ar} = 3,000/1,900/100 \text{ ml}/(\text{g}_{\text{cat}}\cdot\text{h})$ ; (red) 290 °C, 2.5 MPa,  $\text{SV: H}_2/\text{CO}/\text{Ar} = 18,000/11,400/600 \text{ ml}/(\text{g}_{\text{cat}}\cdot\text{h})$ . The chain-growth probability ( $\alpha$ ) was experimentally determined by considering  $\text{C}_3\text{-C}_9$  hydrocarbons obtained from the product effluent after 60 h time on stream.



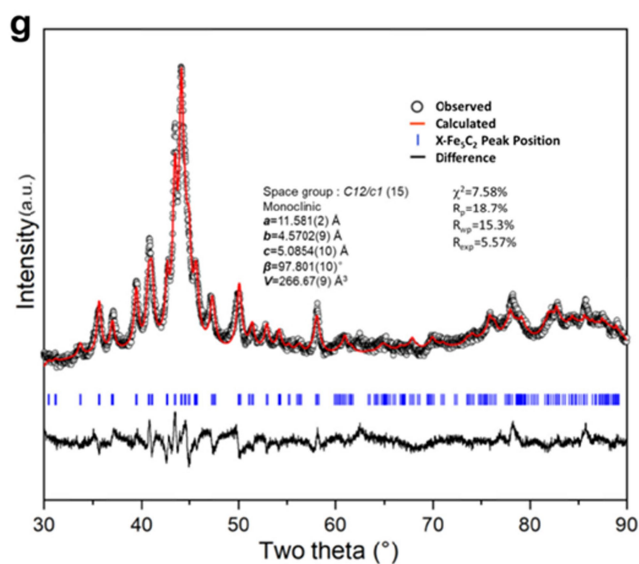
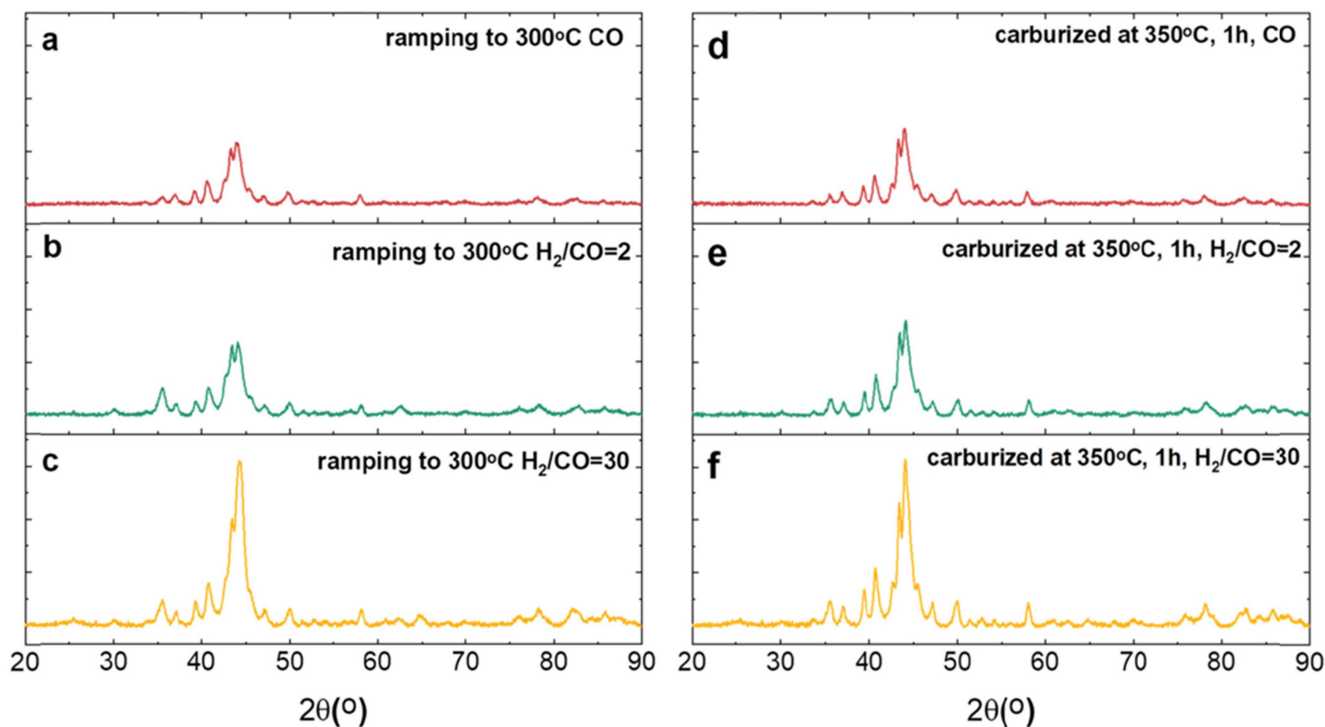


Figure 7(h) presents the atomic parameters for  $\chi$ - $Fe_5C_2$ .

Atomic parameters					
Atom	Wyck.	Site	x/a	y/b	z/c
Fe3	4e	2	0	0.5788(16)	¼
Fe1	8f	1	0.0980(5)	0.0747(17)	0.4134(6)
C1	8f	1	0.10700	0.28500	0.14900
Fe2	8f	1	0.2156(5)	0.5842(14)	0.2909(8)

Figure 7(i) shows the average crystallite sizes determined by Scherrer analysis of the XRD patterns.

	Fe or $\chi$ - $Fe_5C_2$	Mn/Fe or Mn/ $\chi$ - $Fe_5C_2$
Precursor	13 nm	17 nm
Carbide	15 nm	18 nm

**Extended Data Fig. 7 | In situ XRD for unpromoted and Mn-promoted Raney Fe.** XRD patterns obtained (a)-(c) after ramping to 300 °C in CO,  $H_2/CO = 2$  and  $H_2/CO = 30$ , 0.1 MPa, (d)-(f), after subsequent carburization at 350 °C for 1 h under CO,  $H_2/CO = 2$  and  $H_2/CO = 30$ , 0.1 MPa. (g)-(h) Rietveld refinement of

$\chi$ - $Fe_5C_2$  obtained by the optimized carburization procedure:  $H_2/CO = 30$ , 0.1 MPa, 30 °C to 350 °C at 0.5 °C/min, dwell 6 h. (i) Average crystallite sizes determined by Scherrer analysis of the XRD patterns.

Extended Data Table 1 | DFT-computed energetics of FT reaction steps for  $\chi$ -Fe<sub>5</sub>C<sub>2</sub>(100)

Elementary Reaction step			$E_f$ (kJ/mol)	$\nu_f$ (s <sup>-1</sup> )	$E_b$ (kJ/mol)	$\nu_b$ (s <sup>-1</sup> )
C + H	→	CH	78	$1.4 \cdot 10^{13}$	97	$1.3 \cdot 10^{13}$
CH + H	→	CH <sub>2</sub>	53	$5.8 \cdot 10^{13}$	12	$8.9 \cdot 10^{12}$
CH <sub>2</sub> + H	→	CH <sub>3</sub>	49	$9.1 \cdot 10^{13}$	45	$3.0 \cdot 10^{12}$
CH <sub>3</sub> + H	→	CH <sub>4</sub>	109	$1.7 \cdot 10^{13}$	49	$1.3 \cdot 10^{11}$
CO + O	→	CO <sub>2</sub>	181	$4.3 \cdot 10^{13}$	142	$7.6 \cdot 10^{13}$
O + H	→	OH	65	$7.3 \cdot 10^{13}$	46	$8.6 \cdot 10^{12}$
OH + H	→	H <sub>2</sub> O	136	$1.6 \cdot 10^{13}$	1	$1.5 \cdot 10^{12}$
OH + OH	→	H <sub>2</sub> O + O	118	$6.4 \cdot 10^{12}$	1	$5.1 \cdot 10^{12}$
CO + OH	→	COOH	166	$7.7 \cdot 10^{12}$	16	$2.3 \cdot 10^{13}$
COOH	→	CO <sub>2</sub> + H	136	$2.5 \cdot 10^{13}$	27	$5.0 \cdot 10^{12}$
C + C	→	CC	90	$4.6 \cdot 10^{11}$	110	$7.9 \cdot 10^{12}$
C + CH	→	CCH	79	$1.9 \cdot 10^{12}$	88	$7.9 \cdot 10^{12}$
C + CH <sub>2</sub>	→	CCH <sub>2</sub>	122	$2.2 \cdot 10^{12}$	174	$1.0 \cdot 10^{13}$
C + CH <sub>3</sub>	→	CCH <sub>3</sub>	96	$1.1 \cdot 10^{13}$	80	$1.3 \cdot 10^{13}$
CH + CH	→	CHCH	117	$2.0 \cdot 10^{11}$	138	$6.6 \cdot 10^{11}$
CH + CH <sub>2</sub>	→	CHCH <sub>2</sub>	111	$1.4 \cdot 10^{13}$	88	$2.2 \cdot 10^{13}$
CH + CH <sub>3</sub>	→	CHCH <sub>3</sub>	181	$2.5 \cdot 10^{12}$	128	$4.5 \cdot 10^{12}$
CH <sub>2</sub> + CH <sub>2</sub>	→	CH <sub>2</sub> CH <sub>2</sub>	112	$1.1 \cdot 10^{13}$	128	$1.6 \cdot 10^{12}$
CH <sub>2</sub> + CH <sub>3</sub>	→	CH <sub>2</sub> CH <sub>3</sub>	124	$8.0 \cdot 10^{12}$	101	$7.6 \cdot 10^{13}$
CC + H	→	CCH	70	$1.6 \cdot 10^{13}$	77	$1.4 \cdot 10^{13}$
CCH + H	→	CCH <sub>2</sub>	45	$1.9 \cdot 10^{13}$	47	$1.2 \cdot 10^{13}$
CCH + H	→	CHCH	67	$1.8 \cdot 10^{13}$	61	$1.8 \cdot 10^{13}$
CCH <sub>2</sub> + H	→	CCH <sub>3</sub>	42	$6.4 \cdot 10^{12}$	6	$5.8 \cdot 10^{11}$
CCH <sub>2</sub> + H	→	CHCH <sub>2</sub>	142	$5.6 \cdot 10^{13}$	85	$6.8 \cdot 10^{13}$
CHCH + H	→	CHCH <sub>2</sub>	103	$1.5 \cdot 10^{13}$	55	$1.2 \cdot 10^{13}$
CCH <sub>3</sub> + H	→	CHCH <sub>3</sub>	56	$2.8 \cdot 10^{12}$	1	$2.0 \cdot 10^{12}$
CHCH <sub>2</sub> + H	→	CH <sub>2</sub> CH <sub>2</sub>	38	$3.3 \cdot 10^{13}$	36	$4.7 \cdot 10^{12}$
CHCH <sub>2</sub> + H	→	CHCH <sub>3</sub>	200	$1.3 \cdot 10^{14}$	165	$6.6 \cdot 10^{12}$
CH <sub>2</sub> CH <sub>2</sub> + H	→	CH <sub>2</sub> CH <sub>3</sub>	48	$6.3 \cdot 10^{12}$	4	$1.9 \cdot 10^{13}$
CHCH <sub>3</sub> + H	→	CH <sub>2</sub> CH <sub>3</sub>	57	$2.0 \cdot 10^{12}$	45	$1.7 \cdot 10^{13}$
CH <sub>2</sub> CH <sub>3</sub> + H	→	CH <sub>3</sub> CH <sub>3</sub>	94	$2.5 \cdot 10^{14}$	139	$7.5 \cdot 10^{13}$

Activation energies and pre-exponential factors for methane formation, oxygen removal reactions, ethylene and ethane formation.

Extended Data Table 2 | Kinetic study for Mn-promoted FTLO catalyst

SV (ml/g <sub>cat</sub> /h)	T (°C)	X <sub>CO</sub> (%)	S <sub>CO2</sub> (%)
90000	250	11.6	6.9
75000	250	14.5	6.4
60000	250	17.2	6.3
30000	250	25.5	6.6
90000	270	21.6	11.0
75000	270	23.8	11.6
60000	270	26.3	12.7
30000	270	38.0	13.1
90000	290	39.4	18.6
75000	290	42.2	20.5
60000	290	48.9	20.5
30000	290	67.9	21.7
90000	310	60.1	28.1
75000	310	64.5	28.8
60000	310	69.9	28.6

CO conversion and CO<sub>2</sub> selectivity for Mn- $\chi$ -Fe<sub>3</sub>C<sub>2</sub> catalyst under various reaction conditions (fixed-bed reactor, pressure 2.5MPa, H<sub>2</sub>/CO=1.5, no diluent gas added). The Mn promoter content is 10wt%.

**Extended Data Table 3 | In situ Mössbauer spectra for FTLO catalysts**

<i>Sample/ Treatment</i>	<i>T (K)</i>	<i>IS (mm·s<sup>-1</sup>)</i>	<i>QS (mm·s<sup>-1</sup>)</i>	<i>Hyperfine field (T)</i>	<i>Γ (mm·s<sup>-1</sup>)</i>	<i>Phase</i>	<i>Spectral contribution (%)</i>
Raney Fe	4.2	0.01	-	33.9	0.36	Fe <sup>0</sup>	64
Passivated		0.33	-0.01	49.0	0.47	Fe <sup>3+</sup>	36
H <sub>2</sub> /CO/He=	4.2	0.26	-	25.0	0.48	χ-Fe <sub>5</sub> C <sub>2</sub> (I)	42
100/3.2/21.8		0.18	-	21.8	0.50	χ-Fe <sub>5</sub> C <sub>2</sub> (II)	38
350 °C, 40 min		0.14	-	13.9	0.47	χ-Fe <sub>5</sub> C <sub>2</sub> (III)	20
H <sub>2</sub> /CO/He=	120	0.26	-	24.6	0.41	χ-Fe <sub>5</sub> C <sub>2</sub> (I)	41
100/3.2/21.8		0.19	-	21.3	0.44	χ-Fe <sub>5</sub> C <sub>2</sub> (II)	39
350 °C, 6 h		0.16	-	13.6	0.41	χ-Fe <sub>5</sub> C <sub>2</sub> (III)	20
H <sub>2</sub> /CO=1.5	120	0.26	-	24.5	0.39	χ-Fe <sub>5</sub> C <sub>2</sub> (I)	41
water saturator		0.19	-	21.1	0.41	χ-Fe <sub>5</sub> C <sub>2</sub> (II)	38
265 °C, 2.3 MPa, 12 h		0.16	-	13.4	0.40	χ-Fe <sub>5</sub> C <sub>2</sub> (III)	21
Mn /Raney Fe	4.2	-0.01	-	34.1	0.43	Fe <sup>0</sup>	64
Passivated		0.35	-0.01	47.4	0.56	Fe <sup>3+</sup>	31
		0.34	1.30	-	0.73	Fe <sup>3+</sup>	5
H <sub>2</sub> /CO/He=	4.2	0.25	-	24.6	0.45	χ-Fe <sub>5</sub> C <sub>2</sub> (I)	47
100/3.2/21.8		0.18	-	21.6	0.47	χ-Fe <sub>5</sub> C <sub>2</sub> (II)	36
350 °C, 40 min		0.14	-	13.7	0.46	χ-Fe <sub>5</sub> C <sub>2</sub> (III)	17
H <sub>2</sub> /CO/He=	120	0.25	-	24.7	0.44	χ-Fe <sub>5</sub> C <sub>2</sub> (I)	46
100/3.2/21.8		0.18	-	21.7	0.48	χ-Fe <sub>5</sub> C <sub>2</sub> (II)	37
350 °C, 6 h		0.15	-	13.7	0.44	χ-Fe <sub>5</sub> C <sub>2</sub> (III)	17
H <sub>2</sub> /CO=1.5	120	0.25	-	24.7	0.45	χ-Fe <sub>5</sub> C <sub>2</sub> (I)	47
water saturator		0.18	-	21.6	0.47	χ-Fe <sub>5</sub> C <sub>2</sub> (II)	36
265 °C, 2.3 MPa, 12 h		0.14	-	13.8	0.47	χ-Fe <sub>5</sub> C <sub>2</sub> (III)	17

Fitting results of in situ Mössbauer spectra of the transformation of unpromoted and Mn-promoted Raney Fe to phase-pure χ-Fe<sub>5</sub>C<sub>2</sub>.

Experimental uncertainties: Isomer shift: I.S. ± 0.02 mm s<sup>-1</sup>; Quadrupole splitting: Q.S. ± 0.02 mm s<sup>-1</sup>; Line width: Γ ± 0.03 mm s<sup>-1</sup>; Hyperfine field: ± 0.1 T; Spectral contribution: ± 3%.